Beam shaping with segmented devices

Author:
Lehloa Mohapi

Supervisor:
Dr. Angela Dudley

Co-supervisor:
Prof. Andrew Forbes

A thesis submitted in fulfillment of the requirements for the degree of Master of Science

in the

Structured Light Laboratory
School of Physics

January 20, 2023

Declaration of Authorship

I, Lehloa MOHAPI, declare that this thesis titled, "Beam shaping with segmented devices" and the work presented in it are my own. I confirm that:

- This work was done wholly or mainly while in candidature for a research degree at this University.
- Where any part of this thesis has previously been submitted for a degree or any other qualification at this University or any other institution, this has been clearly stated.
- Where I have consulted the published work of others, this is always clearly attributed.
- Where I have quoted from the work of others, the source is always given. With the exception of such quotations, this thesis is entirely my own work.
- I have acknowledged all main sources of help.
- Where the thesis is based on work done by myself jointly with others, I have made clear exactly what was done by others and what I have contributed myself.

Signed:

Date:

"Build me a son, O Lord, who will be strong enough to know when he is weak, and brave enough to face himself when he is afraid, one who will be proud and unbending in honest defeat, and humble and gentle in victory."

Douglas MacArthur

UNIVERSITY OF THE WITWATERSRAND

Abstract

Faculty of Science
School of Physics

Master of Science

Beam shaping with segmented devices

by Lehloa MOHAPI

The ability to tailor light in all its degrees of freedom has led to various applications in fields such as medical technology, industrial, military and free-space communication. While a surfeit of techniques exists to shape light such as the spatial light modulator (SLM), diffractive optical elements (DOEs), and deformable mirrors to name a few, high-power beam shaping is still a challenge. DOEs and the deformable mirrors are beneficial due to their ability to shape high power beams, however, they are costly and complex to fabricate. We use a liquid crystal on silicon spatial light modulator (LCoS-SLM) to investigate the minimal amount of steps or segments required to shape a phase of interest with high fidelity. In Chapter 3 we illustrate that we only require 10 multi-level steps to generate high fidelity phase structures for orbital angular momentum phase (vortex beam), cubic phase (Airy beam) and axicon phase (Bessel beam in the near-field and annular ring in the far-field) as examples. In Chapter 4 we show a relationship between the segmented modulator geometry and the transverse phase structure. Various phase structures with phase configurations were demonstrated, the segments geometry that matches the geometry of the phase structure requires less segments to align with the phase discontinuities. We also demonstrate how rotating the phase of a non-symmetric phase structure may affect the fidelity of a beam profile. This work will serve as a guide to those who wish to simulate first with the LCoS-SLM before the physically fabricate the aforementioned devices for beam shaping.

Acknowledgements

To my Parents, thank you for being my anchor and shoulder to cry on whenever the road seemed steep and impossible, you are the best. To my siblings Ntsa and Nyane, I would never trade both of you for better siblings, you are both phenomenon. A special appreciation to Charmaine Manabile, The sleepless nights you had just to listen to my presentations before every conference I attended have been one of the joyous moments of my life. To my friends, Boitumelo Pekesha, Keabetswe Pholoana, Olebogeng Baloyi and Thato Mohapi, you all helped me sustain the vision I always had, and now it has become a reality. I am in awe of the love and support you all showed me. A special thanks goes to the "Structured light group", Dr Wagner Buono, not only are you my mentor, you have been a dear brother whom I look up to. Always be who you are, kind genuine and smart. Dr Isaac Nape and soon to be Dr Bereneice Sephton, It goes without saying that both of you played a huge role both academically and socially, thank you. Keshaan Singh, Pedro ornelas, Leerin Perumal, Cade Peters, Ashley Phala, Ané Kritzinger, Chané Moodley, and Stirling Scholes you are all amazing and I would be lying if I said I did it all by myself. You all played a huge role, socially and academically, your kind gestures will forever be in my heart. I love every single one of you. To my academic parents, Prof Andrew Forbes and Dr Angela Dudley, you both gave me an opportunity of a lifetime and I can never thank you both enough for what you have done for me. I admire and look up to both of you. Everyone has that one coach who played a huge role in their success, I am honoured and privileged to have two coaches. I will forever walk tall and proud knowing that I had two great giants on my corner. Finally, above all, I would like to thank God who continues to carry me through my accomplishments.

Contents

List of Figures

Dedicated to my family. What a long and twisted road it's been...

Chapter 1

Introduction

Beam shaping is defined as the ability to tailor a laser beam in all its degrees of freedom (DoFs), that is its phase, amplitude and polarisation of light. Early beam shaping involved the conversion of a Gaussian beam into a beam with uniform intensity profile for industrial applications which includes laser cutting and laser welding [1]. Unlike the Gaussian beam, the flattop beam has constant intensity, and beside mapping techniques, it can be generated by resonators limiting the transverse extent of the beam while exploiting the beam's maximum energy output.

Modern beam shaping involve the use of computer controlled micro-display devices known as spatial light modulators (SLMs) to convert an incident Gaussian beam into various spatial profiles through the use of a computer generated hologram (CGH) [2]–[4]. An SLM is any device that can be configured dynamically in real-time to alter a laser beam in all its DoFs to generate an output intensity profile in the desired observation plane [5]–[8]. SLMs offers great opportunities in various applications (some of which are outlined by Neil Savage [9]) due to their technological advancements which includes fast response time, they are less bulky, they produce high image resolution, and they are relatively cheaper than some conventional technologies like the macro scaled deformable mirrors [10].

There are different types of SLMs which are divided into two classes: The microelectromechanical (MEMS) based SLMs such as the micro-actuated deformable mirrors [11]–[14] and the MEMS based digital micromirror devices (DMDs) [15], [16], these two types of MEMS based devices are made up of a number of movable micromirrors attached to the actuators which are controlled by the electric field. A deformable mirror may have a piston only actuation, where each micromirror is attached to a single actuator responsible to deform the reflective surface through an up or down actuation. Deformable mirror can also be configured with a tip-tilt movement, where each mirror is attached to two or three actuators responsible to tip and tilt the reflective surface and mimic deformable mirrors made of a continuous reflective surface. Even though they are more costly than their piston-only counterparts, due to the number of actuators they posses, they also prevent energy loss as result of diffraction that often occurs in a piston-only movement [17]. The MEMS based deformable mirrors are quite different because their segmented micromirros are fabricated for a tilt-only movement.

Other SLM devices that are commonly used for beam shaping are the MEMS based DMDs and the liquid crystal on silicon (LCoS) SLMs. The former is an imitative micro-display version of a deformable mirror device which was invented in 1987 by Hornberk, who at that time was working for Texas Instruments [18]. The latter is a widely used micro-display based on LCoS, and unlike other SLMs, the LCoS-SLMs is able to produce higher image resolution in both phase and amplitude due to its controllable pixelated liquid crystal display (LCD) [19]. LCoS-SLM was envisioned and designed at Hughes Aircraft corporation in the seventies which up to today has lived to its expectations as one of the widely used and successful SLM [20].

Both LCoS-SLMs and MEMS based DMDs have been widely used to mimic some optical elements such as conical lenses, spiral phase plates, q-plates, and even cylindrical lenses to reduce optical fabrication costs and time and for a more dynamic and adaptable beam shaping techniques. For example more exotic laser beams have been successfully generated, such as vortex beams [21]–[23], Bessel beams [24]–[26], flat-top beams [27] and Airy beams [28] to name a few, one only needs to fine tune holographic algorithms onto the micro-display device to switch between beams. They are also used to mimic adaptive optics to correct for optical abberations present in an incoming wavefront [29], [30]. Another technology used for phase modulation are diffractive optical elements (DOEs) [31]. DOEs are made up of surface relief patterns as a result of phase masks based on lithographic film plates etched onto a substrate (e.g glass substrate) which are fabricated for a specific laser beam shaping. Depending on the etching iteration steps conducted, a certain amount of efficiency is directed into the 1^{st} desired order.

The history and development of these devices goes as far as the discovery of diffraction of light in 1665 by a mathematician Francesco Grimaldi [32]. Grimaldi observed fringes (interference pattern) of light in the shadow of a rod incident by a light source. He was the first to realise the tendency of light to bend as it passes through an obstacle and he named this phenomenon "diffraction".

An English scientist Robert Hooke also realised diffraction patterns appearing at thin film, however at that time there was no explanation as to why there were numerous colored patterns of interference caused by white light [33]. Hooke did not understand that light (depending on the wavelength) bend differently as it passes through an obstacle that is smaller or equal to the wavelength of light passing through it. The nature of diffraction made a breakthrough in 1802 which gave a solution to Hooke's light diffraction problem when Thomas Young introduced and demonstrated the principle of light interference patterns through a double slit experiment. He used the sun as a light source and he witnessed different light colored fringes appeared on the thin film [34], [35]. This occurred because light bends differently depending on the size of the slit or aperture the light goes through. In this case the double slits had different wavelength spacing that divided the light wavelengths in different angles.

This gave birth to traces of DOEs that are reviewed in Chapter 3. The advantage of using DOEs for phase modulation is the ability to obtain a 100% efficiency in the desired order, an example is by using a blazed grating [36]. Some DOEs are difficult to fabricate, in this case an approximation has to be used to generate a device through a binary or multi-level technique, for example in the case of a binary grating or a blazed grating respectively [37]. The former is based on two level discrete phase approximation and is often not required for much complex approximations like the Fresnel lens which requires more than two level phase approximation to achieve close to a 100% efficiency in the desired order.

The disadvantage of this technique is often knowing the number of phase-masks required prior to fabrication for a specific phase modulation pattern, which may lead to more than required phase masks resulting in high expenditure and unnecessary time consumption. Since the LCoS-SLMs consist of pixels which can be dynamically addressed to modulate the phase and structure of an incident beam into various phase profiles they have received enormous attention as pattern generators[38].

In Chapter 3 and Chapter 4, we use the LCoS-SLM as a testbed to explore and mimic optical devices based on diffractive and reflective devices. The former is the device used to generate diffractive optical structures in a multi-level discrete way, which can either be phase masks or resist depths in the case of multi-level DOEs or the number of mirror segments, as well as mirror geometries in the case of deformable mirrors. The ability to select before physical fabrication the lowest possible segmented iterations that can produce high fidelity spatial profiles will reduce the cost and time of fabrication.

1.1 Paraxial wave equation

Maxwell formulated four equations with each equation broken down into three dimensional planes (x, y, z) to explain the relationship between the electric and magnetic fields, which we know today as electromagnetic (EM) fields propagating in free space [39], [40]. The equations will help us derive the Helmholtz wave equation which describes the propagation of electromagnetic waves in three dimensions (using the x,y,z basis) [41]. Using the Helmholtz wave equation we will then be able to derive the paraxial Helmholtz wave equation to find solutions in cylindrical and Cartesian coordinates for some generated modes in free-space. We begin with Maxwell's equations below

$$\vec{\nabla} \cdot \vec{E} = \frac{\rho}{\epsilon_0}, \tag{1.1}$$

$$\vec{\nabla} \cdot \vec{B} = 0, \tag{1.2}$$

$$\vec{\nabla} \times \vec{E} = -\frac{\partial \vec{B}}{\partial t}, \tag{1.3}$$

$$\vec{\nabla} \times \vec{B} = \epsilon_0 \mu_0 \frac{\partial \vec{E}}{\partial t} + \mu_0 \vec{j}, \tag{1.4}$$

where

$$\epsilon_0 \mu_0 = \frac{1}{c^2}. \tag{1.5}$$

In the above equations ρ and $\vec{j}$ are the charge density and the vector current density respectively, t is time in seconds and $\vec{\nabla}$ denotes the three-dimensional gradient operator. The vectors $\vec{E}$ and $\vec{B}$ are the electric field and magnetic field displacements respectively and ϵ_0, μ_0 are the electric and magnetic permeability of free-space respectively which are constants. In equation 1.5 c is the speed of light, taking the curl of equation 1.3, we have

$$\vec{\nabla} \times \left(\vec{\nabla} \times \vec{E}\right) = -\vec{\nabla} \times \frac{\partial \vec{B}}{\partial t}. \tag{1.6}$$

Using the cross vector product rule, equation 1.6 becomes

$$\vec{\nabla} \times \left(\vec{\nabla} \times \vec{E}\right) = -\frac{\partial}{\partial t}\left(\vec{\nabla} \times \vec{B}\right). \tag{1.7}$$

It is important to note that the curl of the magnetic field in equation 1.7 is the fourth Maxwell's magnetism equation. When electromagnetic waves propagate in a vacuum, there is no induced sources of charges or currents

$$\rho = 0, \tag{1.8}$$

$$\vec{j} = 0. \tag{1.9}$$

By substituting equation 1.4 into equation 1.7 we obtain

$$\vec{\nabla} \times \left(\vec{\nabla} \times \vec{E}\right) = -\frac{1}{c^2}\frac{\partial}{\partial t}\frac{\partial \vec{E}}{\partial t}. \tag{1.10}$$

If we begin first with the easier partial derivative of the electric field with respect to time and with the knowledge of the second order partial derivative, the term on the right hand sign of equation 1.10 will have the following expression

$$-\frac{1}{c^2}\frac{\partial}{\partial t}\frac{\partial \vec{E}}{\partial t} = -\frac{1}{c^2}\frac{\partial^2 \vec{E}}{\partial t^2}. \tag{1.11}$$

On the left hand sign of equation 1.10, a curl of a curl has a known expression

$$\vec{\nabla} \times \left(\vec{\nabla} \times \vec{E}\right) = \vec{\nabla}(\vec{\nabla} \cdot \vec{E}) - \nabla^2 \vec{E}, \tag{1.12}$$

where $\vec{\nabla}\left(\vec{\nabla}.\vec{E}\right)$ is the gradient of the divergence of $\left(\vec{E}\right)$ and $\nabla^2\,\vec{E}$ is the Laplacian of a vector $\left(\vec{E}\right)$. In a vacuum the divergence of $\vec{E}$ in equation 1.1 is zero because the charge density does not exist in such medium. Equation 1.12 assumes the following form:

$$\vec{\nabla} \times \left(\vec{\nabla} \times \vec{E}\right) = -\nabla^2 \vec{E}. \tag{1.13}$$

Finally, bringing the two solutions together gives the following result:

$$\nabla^2 \vec{E} = \frac{1}{c^2}\frac{\partial^2 \vec{E}}{\partial t^2}. \tag{1.14}$$

The wave equation is therefore

$$\nabla^2 \vec{E} - \frac{1}{c^2}\frac{\partial^2 \vec{E}}{\partial t^2} = 0. \tag{1.15}$$

Now that the wave equation is derived elegantly, we have to use the wave equation to derive the Paraxial approximation. Consider the following expression,

$$\vec{E} = E\,(x, y, z)\exp\left(-ikz\right)\exp\left(-i\omega t\right)\hat{x}, \tag{1.16}$$

$\hat{x}$ implies that the electric field with amplitude $E\,(x, y, z)$ is linearly polarized along the x-direction, where ω and k are the wave frequency and the wave number respectively given by,

$$\omega = \frac{2\pi c}{\lambda}, \tag{1.17}$$

where

$$k = \frac{2\pi}{\lambda}. \tag{1.18}$$

We assume that equation 1.16 is the electric field for monochromatic light traveling along the propagation direction z. We then substitute the electric field of equation 1.16 into the wave equation,

$$\nabla^2 \left(E\left(x,y,z\right)\exp\left(-i\left(kz+\omega t\right)\right)\right) - \frac{\partial^2 (E(x,y,z)\exp\left(-i\left(kz+\omega t\right)\right)}{\partial t^2}\frac{1}{c^2} = 0. \tag{1.19}$$

Completing the second partial derivative with respect to time (t) in equation 1.19 we obtain

$$\nabla^2 \left(E\left(x,y,z\right)\exp\left(i\left(kz+\omega t\right)\right)\right) - \omega^2 \exp\left(i\left(kz+\omega t\right)\right)\frac{1}{c^2} = 0, \tag{1.20}$$

from equation 1.17 and equation 1.18, equation 1.20 reduces to the following equation

$$\nabla^2 \left(E\left(x,y,z\right)\exp\left(i\left(kz+\omega t\right)\right)\right) - k^2 \exp\left(i\left(kz+\omega t\right)\right) = 0. \tag{1.21}$$

The Laplace operator has a known identity,

$$\nabla^2 = \frac{\partial^2}{\partial x^2} + \frac{\partial^2}{\partial y^2} + \frac{\partial^2}{\partial z^2}, \tag{1.22}$$

$$\left(\frac{\partial^2}{\partial x^2} + \frac{\partial^2}{\partial y^2} + \frac{\partial^2}{\partial z^2}\right)\left(E\left(x,y,z\right)\exp\left(i\left(kz+\omega t\right)\right)\right) + \omega^2 \exp\left(i\left(kz+\omega t\right)\right) = 0. \tag{1.23}$$

By using the product rule

$$\frac{\partial^2}{\partial x^2}\left(f\left(x\right)g\left(x\right)\right) = \frac{\partial}{\partial x}\left(\frac{\partial f\left(x\right)}{\partial x}g\left(x\right) + \frac{\partial g\left(x\right)}{\partial x}f\left(x\right)\right), \tag{1.24}$$

equation 1.23 reduces to the following equation

$$\left(\frac{\partial^2}{\partial x^2} + \frac{\partial^2}{\partial y^2} + \frac{\partial^2}{\partial z^2}\right)\left(E\left(x,y,z\right)\exp\left(-i\left(kz+\omega t\right)\right)\right) - 2ik\frac{\partial E\left(x,y,z\right)}{\partial z}\exp\left(-i\left(kz+\omega t\right)\right) = 0. \tag{1.25}$$

If we divide equation 1.25 by the phase term $\exp\left(-i\left(kz+\omega t\right)\right)$, we arrive at

$$\left(\frac{\partial^2}{\partial x^2} + \frac{\partial^2}{\partial y^2} + \frac{\partial^2}{\partial z^2}\right)E\left(x,y,z\right) - 2ik\frac{\partial E\left(x,y,z\right)}{\partial z} = 0. \tag{1.26}$$

For an electric field that spreads very slowly along the propagation direction z, the second partial derivative $\frac{\partial^2 E(x,y,z)}{\partial z^2}$ can be ignored since the angular spread is so small it is negligible [42],

$$\left|\frac{\partial^2 E(x,y,z)}{\partial z^2}\right| << \left|2ik\frac{\partial E(x,y,z)}{\partial z}\right|, \tag{1.27}$$

and with the assumption in equation 1.27 we have reduced the equation to the paraxial equation given by,

$$\left(\frac{\partial^2}{\partial x^2}+\frac{\partial^2}{\partial y^2}\right)E\left(x,y,z\right)-2ik\frac{\partial E\left(x,y,z\right)}{\partial z}=0. \tag{1.28}$$

In equation 1.28, the second order partial derivatives with respect to x and y can be written compactly as,

$$\frac{\partial^2}{\partial x^2}+\frac{\partial^2}{\partial y^2}=\nabla_T^2, \tag{1.29}$$

where ∇_T^2 is the Laplacian in the transverse direction, and so equation 1.28 will result in

$$\nabla_T^2 E\left(x,y,z\right)-2ik\frac{\partial E\left(x,y,z\right)}{\partial z}=0. \tag{1.30}$$

By solving the paraxial wave equation in cylindrical coordinates we obtain Laguerre-Gaussian modes carrying a well defined Orbital Angular Momentum (OAM) and by solving the equation in cartesian coordinates we obtain Hermite-Gaussian modes [43].

1.2 Gaussian beam

Gaussian beams are laser beams that posses an electromagnetic radiation that is described by a Gaussian distribution function, hence the bell-shaped $1D$ intensity distribution seen in figure 1.1. The bell shaped profile is due to the maximum intensity seen in the center of the beam which decreases and approaches zero as we move away from the center. These beams have the simplest transverse electromagnetic mode (TEM_{00}) which have the most desirable irradiance found in laser sources, and they are also used as a solution to other higher order spatial beams. They are a solution to the paraxial wave equation and therefore they are propagation invariant in nature.

The electric field of the Gaussian beam is given by

$$E(r,z)=\frac{\omega_0}{\omega(z)}\exp\left(\left(-\frac{r}{\omega(z)}\right)^2\right)\exp\left(\left(-ik\frac{r^2}{2R(z)}-i\psi(z)\right)\right), \tag{1.31}$$

where ω_0 is the beam waist when $\omega(z)=\omega_0$, $R(z)$ is the radius of curvature given by

$$R(z)=z\left[1+\left(\frac{z_R}{z}\right)^2\right], \tag{1.32}$$

and $\psi(z)$ is the Gouy phase given by

$$\psi(z)=\arctan\left(\frac{z}{z_R}\right), \tag{1.33}$$

the term $z_R=\frac{\pi\omega_0^2}{\lambda}$ is the Rayleigh range. Consider a Gaussian beam propagating through a lens of some arbitrary focal length with a beam radius given by

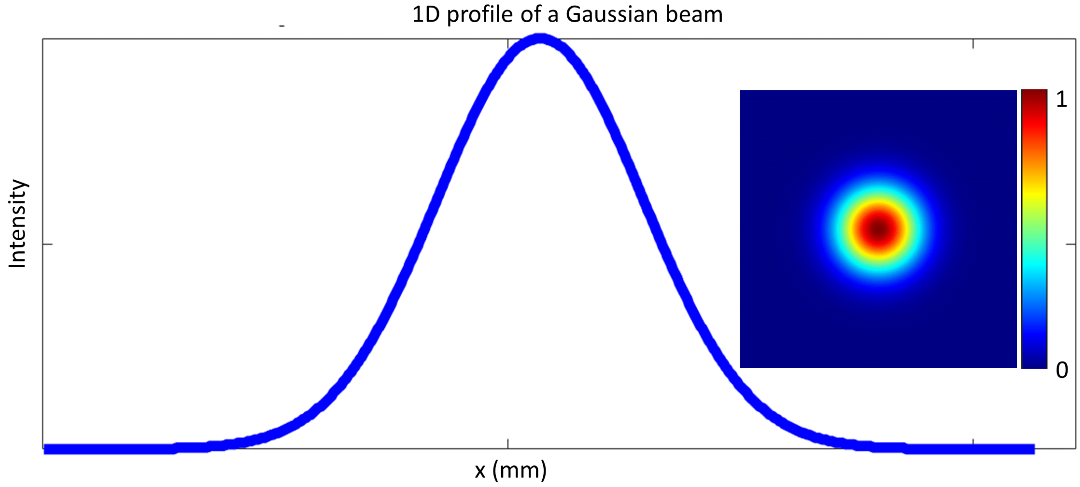

FIGURE 1.1: A $2D$ Gaussian beam intensity profile with intensity profile that drops and asymptotically approaches zero away from the central maxima with a $1D$ corresponding intensity profile at the bottom. The $1D$ Gaussian beam intensity profile is identified with a bell-shaped Gaussian distribution with the maximum intensity at the peak of the distribution curve.

$$\omega(z) = \omega_0 \sqrt{1 + \left(\frac{z}{z_R}\right)^2}, \tag{1.34}$$

when $z = 0$, we obtain the $2D$ intensity profile in figure 1.1 given by the absolute squared of the electric field expressed by

$$I(r) = |E(r)|^2 = \frac{2P}{\pi\omega_0^2} \exp\left(-2\left(\frac{r}{\omega_0}\right)^2\right), \tag{1.35}$$

where P is the power of the Gaussian beam at the beam waist, which is at its maximum. At any region prior or beyond the beam waist $\omega(z) \neq \omega_0$ and ω_0 in equation 1.35 is replaced by $\omega(z)$.

1.3 Orbital Angular Momentum of light

When scientists explored the electromagnetic nature of light, it was realised that the electromagnetic field can be circularly polarised which carries with it an angular momentum that can either be a spin angular momentum (SAM) or an orbital angular momentum (OAM) [44], [45], the latter will be the focus of this section. Any light that has an azimuthal phase dependence of [46]

$$E(r, z) = \exp(i\ell\phi), \tag{1.36}$$

is known as an OAM mode or a beam that carries OAM, where ϕ is the azimuthal angle and ℓ is known as the azimuthal index, OAM number or the topological charge. The topological charge can assume either a negative or a positive value which can range from $\ell = (-\infty, ..., -1, 0, 1, ..., \infty)$, the change in the (ℓ) signs just changes the direction twist of the wavefront helicity and not the intensity profile of the beam. When $\ell = 1$ the wavefront will twist in a clockwise direction and when $\ell = -1$ the wavefront will twist in an anti-clockwise direction.

In 1884 an English physicist John Henry Poynting discovered a quantity used to describe the size and direction of the flow of energy in electromagnetic waves. We will use the Poynting vector to show that there is a direct proportionality between the OAM density and the topological charge. The Poynting vector [47] is given by:

$$\vec{S} = \frac{1}{\mu_0}\left(\vec{E} \times \vec{B}\right). \tag{1.37}$$

Electromagnetic waves carry energy as they propagate, for instance, if one focuses sunlight at an object say a piece of paper for a long time, you will notice smoke coming off of the paper and this is evidence enough that light has energy. Another example is lying on the beach sand, the sun radiation begins by warming us after a cold swim and if you lie long enough, you will experience an uncomfortable burning sensation and this is due to electromagnetic radiation. Since electric and magnetic fields are orthogonal to each other, this means that they have equal amounts of energy stored in them, and we are going to prove that. Consider a charged parallel plate capacitor with two oppositely charged plates separated by a distance (d) and having an area (A), the capacitor will induce an electric field $\left(\vec{E}\right)$ between these two plates. The strength of the capacitor will depend on how much electric charge is stored in the capacitor [48], [49]. The capacitor has the following expression,

$$C = \frac{q}{V} = \epsilon_0 \frac{A}{d}, \tag{1.38}$$

where C is the capacitance, q is the charge, V is the voltage induced and ϵ_0 retains its previous definition. For a capacitor to produce an electric field, there must be energy in the system given by:

$$E_C = \frac{1}{2}CV^2. \tag{1.39}$$

The electric field can be defined as the voltage induced in the capacitor divided by the separation distance between the charged plates,

$$E = \frac{V}{d}. \tag{1.40}$$

Substituting equation 1.38 and 1.40 into equation 1.39, and making V in equation 1.40 the subject of the formula to solve the total energy in the capacitor, we obtain:

$$E_C = \frac{1}{2}\epsilon_0 A d E^2 \tag{1.41}$$

where the term Ad gives the volume of a capacitor,

$$\frac{E_C}{vol} = \frac{1}{2}\epsilon_0 E^2. \tag{1.42}$$

Consider again an electric cylindrical solenoid having an area (A) with length (L) and N rotational coils of the wire, with current flowing which induces a magnetic field around this wire. The direction of the magnetic field inside the solenoid is mathematically determined using the right hand rule and from this we can extract the magnetic flux:

$$\phi_B = L_B I = BAN, \tag{1.43}$$

where L_B is the inductor. The magnetic field is mathematically defined as:

$$B = \mu_0 \frac{N}{L} I, \tag{1.44}$$

where I is the current through the wire μ_0 retains it's previous definition. The Electric Motive Force (ϵ) through the wire is

$$\epsilon = -N \frac{d\phi_B}{dt}, \tag{1.45}$$

to attain the total energy through the wire, we have to integrate the power with respect to time, and this results in:

$$E_B = \frac{1}{2} L_B I^2. \tag{1.46}$$

Substituting equation 1.44 into equation 1.43 we obtain,

$$L_B = \mu_0 \frac{N^2 A}{L}. \tag{1.47}$$

If we solve for I in equation 1.44, we obtain

$$I = \frac{BL}{\mu_0 N}. \tag{1.48}$$

Substituting equation 1.47 and equation 1.48 into equation 1.46 and solving the total magnetic energy in a solenoid, we obtain:

$$E_B = \frac{1}{2\mu_0} B^2 AL \tag{1.49}$$

where the term AL is the total volume of a solenoid

$$\frac{E_B}{vol} = \frac{1}{2\mu_0} B^2. \tag{1.50}$$

Now we have to show that the magnitude of the electric radiation of light is the same as the magnitude of the magnetic radiation of light propagating in free-space.

We know that

$$|B| = \frac{|E|}{c}, \tag{1.51}$$

where c is the speed of light. Using the knowledge in equation 1.51 and rewriting equation 1.50, we obtain:

$$\frac{E_B}{vol} = \frac{1}{2\mu_0 c^2} E^2, \tag{1.52}$$

from equation 1.5

$$c^2 = \frac{1}{\epsilon_0 \mu_0}. \tag{1.53}$$

Substituting equation 1.53 into equation 1.52,

$$\frac{E_B}{vol} = \frac{\epsilon_0}{2} E^2 = \frac{E_E}{vol}. \tag{1.54}$$

We have shown that light carries energy with it. In order to calculate the beam's Poynting vector in equation 1.37, vector potential in the Lorenz gauge is expressed by:

$$\vec{A}(x,y,z) = u(x,y,z)\exp\left(i(kz-\omega t)\hat{x}\right). \tag{1.55}$$

The term $u(x,y,z)$ is the complex amplitude. Both the electric and magnetic fields can be obtained and expressed as the curl of the vector potential $\left[\vec{A}(x,y,z)\right]$

$$\vec{B}(x,y,z) = \nabla \times \vec{A}(x,y,z) = ik\exp\left[i(kz-\omega t)\right]\left[u(x,y,z)\hat{y} + \frac{i}{k}\frac{\partial u(x,y,z)}{\partial y}\hat{z}\right], \tag{1.56}$$

and the electric field results in

$$\vec{E}(x,y,z) = \frac{ic^2}{\omega}\nabla \times \vec{B}(x,y,z) = i\omega\exp\left[i(kz-\omega t)\right]\left[u(x,y,z)\hat{x} + \frac{i}{k}\frac{\partial u(x,y,z)}{\partial y}\hat{z}\right]. \tag{1.57}$$

From the paraxial wave equation, we have to ignore the partial derivative in the z-direction. The solution to the Poynting vector given in equation 1.37 can be found using the real terms in equation 1.56 and equation 1.57, expressed as

$$\vec{E}_{real} = \frac{1}{2}\left(\vec{E} + \vec{E}^*\right), \tag{1.58}$$

and

$$\vec{B}_{real} = \frac{1}{2}\left(\vec{B} + \vec{B}^*\right). \tag{1.59}$$

Equation 1.5 can be expressed as

$$\frac{1}{\mu_0} = \epsilon_0 c^2. \tag{1.60}$$

Substitution equation 1.60 into the Poynting vector in 1.37 we get the time-average Poynting vector with the real electric and magnetic fields in equation 1.58 and 1.59 respectively,

$$\vec{S} = \langle \vec{S}_{real} \rangle = \epsilon_0 c^2 \langle \vec{E}_{real} \times \vec{B}_{real} \rangle. \tag{1.61}$$

The time average Poynting vector becomes

$$\vec{S} = \frac{\epsilon_0 c^2}{4}\left(\vec{E} \times \vec{B}^* + \vec{E}^* \times \vec{B}\right) = \frac{\epsilon_0 \omega c^2}{4}(i(u\nabla u^* - u^*\nabla u) + 2k|u|^2\hat{z}). \tag{1.62}$$

we now apply equation 1.62 to a field that has an amplitude expressed in cylindrical coordinates given by

$$u(r,\phi,z) = u_0(r,z)\exp(il\phi). \tag{1.63}$$

The Poynting vector applied in cylindrical coordinates results in the following:

$$S_r = 0, \tag{1.64}$$

$$S_\phi = \frac{l\omega\epsilon_0 u_0^2}{2r}, \tag{1.65}$$

and

$$S_z = k\epsilon_0 \omega u_0^2. \tag{1.66}$$

The total angular momentum assumes the following expression

$$L_z = \frac{1}{2c^2}(r \times S)_z = \frac{l\omega\epsilon_0 u_0^2}{2c^2}. \tag{1.67}$$

Equation 1.67 clearly shows that the OAM density of a propagating field is directly proportional to the topological charge and it will have a well defined OAM.

1.4 Structured modes possessing orbital angular momentum

1.4.1 Vortex beams

Optical beams that possess a helical or twisting wavefronts about their axis are known as optical vortex beams or singular beams, they include the phase only vortex beams, Laguerre Gaussian beams and Bessel beams. Due to the presence of the topological charge ℓ in the azimuthal phase term, this results in the zero intensity in the screw dislocation area. The helicity of the wavefronts can also be thought of as a twisting corkscrew as the beam propagates along the z direction which results in the ring or doughnut like structure with a dark central hole where the waves at the axis cancels each other. A plethora of techniques exist to shape helical wavefronts with a well defined OAM. One technique is to direct a plane wave beam onto a spiral surface device, such surfaces are known as spiral phase plates [50], [51], other techniques include holographic generation [52], liquid crystal based SLMs [53], spiral Fresnel lenses [54], cylindrical lenses [55], q-plates [56] or even directly from the laser source [57]. They have found numerous applications such as optical tweezing [58], optical communication [59]–[61] and optical imaging [62] to name a few. Vortex beams are generated from a fundamental Gaussian beam when it interacts with an azimuthal phase singularity term. The general function of an electric field that consist of a vortex beam is given by

$$E(r, \phi) = G_0 \exp\left(-i\ell\phi\right), \tag{1.68}$$

where $G_0 = \exp\left(-\left(\frac{r}{\omega_0}\right)^2\right)$ is the Gaussian beam incident on a modulator. The transverse intensity profile of a vortex beam has unwanted and uncontrolled rings around the core intensity profile, these are known as radial modes and they can only be controlled through complex amplitude modulation by generating the Laguerre Gaussian (LG) beam(s), which will be outlined in the next section.

1.4.2 Laguerre Gaussian beams

LG modes are formed by solving the paraxial wave equation in cylindrical coordinates (r, ϕ, z) [44] and their electric field can be described mathematically by the following equation [63],

$$\vec{E}_{\ell,p}(r,\phi,z) = \frac{1}{\omega(z)}\sqrt{\frac{2p!}{\pi(p+|\ell|)!}}\left(\frac{\sqrt{2}\rho}{\omega(z)}\right)^{|\ell|}\exp\left[-\left(\frac{\rho}{\omega}\right)^2\right] lg_p^{|\ell|}\left(\frac{2\rho^2}{\omega^2(z)}\right)$$
$$\exp\left[\left(\frac{ik\rho^2}{2R(z)}\right)\right]\exp(i\ell\phi)\exp[i\psi(p,\ell,z)], \quad (1.69)$$

where p is the radial mode, $\omega(z)$ is the beam diameter, $\omega_0(z)$, z_R, ℓ, k and $R(z)$ keep their previous definitions. In equation 1.69 there is a Gouy phase term $\psi(p,\ell,z)$ which is given by

$$\psi(p,\ell,z) = (2p+|\ell|+1)\arctan\left(\frac{z}{z_R}\right). \quad (1.70)$$

The name *LG* beam comes from the Laguerre polynomials $\left(lg_p^{|\ell|}\right)$ which are placed inside the LG beam function integrated with the Gaussian beam, and they provide the LG beams with a radial mode component when $p \geq 1$. Just like the optical phase-only vortex beam, the LG beam has a null central intensity profile when $\ell \neq 0$ and the number of radial modes implies the number of rings around the core vortex beam, if we refer to Chapter 2 figure 2.10, we see that for $p = 1$ and $\ell = 1$ we get 1 ring around the vortex beam and when $p = 3$ we get 3 concentric rings around the vortex beam and so on. When $\ell = 0$ and $p \geq 1$ we obtain p concentric rings with a central Gaussian beam and concentric ring(s) around the core Gaussian beam. In order to remove the concentric rings around the central Gaussian beam, we have to set the radial mode component to zero as well, such that $\ell = p = 0$.

1.4.3 Bessel-Gaussian beams

Another spatial beam profile that has an azimuthal phase dependence is the Bessel-Gaussian (BG) beams, they are also a solution to the paraxial wave equation. They are of interest due to their non-diffracting nature, therefore they are propagation invariant [64]. In 1987 Durnin discovered the mathematical description that explains the Independence that some types of Bessel solutions have on the propagation direction [65]. In nature, these beams have an infinite number of annular rings which carries an infinite amount of energy with them. Such diffraction free beams cannot be generated experimentally, a good approximation is made by adding the Bessel function with a Gaussian beam and as a result we obtain a BG beam with finite energy [66], [67]. The mathematical expression used to generate the electric field of the BG beams is described as

$$E(\rho,\phi,z) = E_z\frac{\omega_0}{\omega(z)}\exp\left[iz\left(k-\frac{k_r^2}{2k}-\psi(z)\right)\right]\exp(i\ell\phi)J_\ell(\chi)\times$$
$$\exp\left[\left(\frac{-1}{\omega^2(z)}+\frac{ik}{2R(z)}\right)\left(\rho^2+\frac{k_r^2z^2}{k_2}\right)\right], \quad (1.71)$$

where, E_z is the amplitude term, k_r is the radial wave vector and ω_0 retains its definition. In equation 1.71 $J_\ell(\chi)$, where $\chi = \frac{k_r\rho z_R}{iz}$ represents Bessel functions of order ℓ, where ℓ is an integer ≥ 0, such that when $\ell = 0$, we obtain a zeroth order Bessel function that has a central Gaussian maxima and when $\ell \geq 1$ we obtain higher order Bessel function with a core vortex beam.

The first successful generation of the zeroth order BG beam involved the illumination of an annular slit at the back-focal position of a converging lens [68], the interference of the waves as they pass through the converging lens forms a BG beam as a result of an obstacle. However, this method is inefficient as a result most of the intensity from the illuminated beam was blocked by the annular slit [69]. More efficient methods exist to approximate the zeroth order Bessel beam, it was realised that holograms can generate BG beams with much higher efficiency of about 40.5% [70], [71]. Another method involves the use of a diffractive optical element known as an axicon or conical lens, if we illuminate a plane wave onto an axicon, we obtain a zeroth order BG beam, if we desire higher order modes, a plane wave must be replaced with an LG beam [72].One of the most interesting properties the BG beams have besides their diffraction free nature is their ability to self heal or reconstruct their spatial properties (phase and amplitude) after they pass through an obstacle [73], [74].

The maximum propagation distance a BG beam can propagate without changing the beam structure is defined as z_{max}, and is mathematically defined as

$$z_{max} = \frac{2\pi\omega_0}{\lambda k_r} = \frac{\omega_0 k}{k_r}, \tag{1.72}$$

where the radial vector can be expressed in terms of the the conical angle given by

$$k_r = \gamma(n_r - 1)k, \tag{1.73}$$

where n_r is the refractive index of the axicon. In equation 1.73, the radial vector (k_r) is inversely proportional to z_{max}, and this affects the distance a BG beam can propagate while keeping its physical nature. An increase in the conical angle would result in a much shorter distance a BG beam would propagate before it refracts, and a decrease in the conical angle would result in an increase in the propagation distance a BG beam would propagate without diffracting.

1.4.4 Airy beams

Another solution to the paraxial wave equation is the Airy beam, these modes are also non-diffracting and as a result they are propagation invariant. The study of Airy beams has a long history dating back in 1838 when Sir George Biddell Airy first derived the Airy integral which was motivated by the formation of optical caustics [75]. The first Airy waveform occurred in 1979 when Berry and Balazs theoretically demonstrated that on of the solution to the Schrödinger equation could produce a non-spreading Airy wave packet [76]. Airy beams in nature display infinite packets of energy [77], [78] and they can only be experimentally approximated (truncated) while retaining their non-diffractive nature up to a certain propagation distance through the use of a cubic phase mask [78]. Here, the "truncated" Airy beam is generated through modulating the Gaussian beam with the cubic phase by using a LCoS-SLM. Airy beams can be mathematically described by

$$A(s_x, s_y, \xi) = Ai\left[s_x - \left(\frac{\xi}{2}\right)^2\right] Ai\left[s_y - \left(\frac{\xi}{2}\right)^2\right] \exp\left[\frac{i\xi}{2}\left(s_x + s_y - \frac{\xi^2}{3}\right)\right], \tag{1.74}$$

where $Ai\,[\mathrm{Y}]$ represents an Airy function, s_x and s_y are dimensionless transverse coordinates along the x and y planes respectively, given by

$$s_x = \frac{x}{\omega_0}, \tag{1.75}$$

and

$$s_y = \frac{y}{\omega_0}, \tag{1.76}$$

where x and y are the transverse scale parameters. In equation 1.74, we also have a normalised propagation distance (ξ) given by

$$\xi = \frac{z}{kx_0^2}, \tag{1.77}$$

where k is the wave vector. Equation 1.74 represents an Airy beam with infinite energy which cannot be physically generated, however, an approximated equation is achieved by setting the normalised propagation distance to zero ($\xi = 0$) such that we obtain the following expression from [78]

$$A(s_x, s_y) = Ai\left[s_x\right] Ai\left[s_y\right] \exp\left[\frac{s_x + s_y}{\omega_0}\right], \tag{1.78}$$

where the Airy beam energy depends on the input beam waist (ω_0).

Airy beams have shown much interest due to their ability to exhibit a self-healing or structural reconstruction properties [79], [80] as they encounter an obstacle just like Bessel beams. They are also capable to freely accelerate in the absence of external potential [81], which makes them beneficial in applications like micromanipulation [82]–[84], plasma guidance [85], and routing surface plasmon polaritons [86].

1.5 Flattop beams

Another interesting spatial beam with a uniform intensity that drops to zero at the edges are known as flattop beams or top-hat beams. This beam can be divided into into four families: the super-Gaussian, flattened Gaussian, Fermi-Dirac and super Lorentzian [87]. Each family has a different intensity profile normalisation constant and a function, let us consider the super-Gaussian as an example, which is defined as from Ref[87]

$$I(r) = I_0 \exp\left[-2\left(\frac{r}{\omega_{SG}}\right)^{\beta}\right], \tag{1.79}$$

where I_0 is the intensity profile normalisation constant, r is the radial coordinate, and ω_{SG} is the beam size of the super-Gaussian approximation. Note that the parameter β controls the steepness of the super-Gaussian beam, for example, when $\beta = 2$, we obtain a Gaussian intensity profile as shown in figure 1.2 (a), when $\beta = 10$, the maximum peak of (a) becomes flatter with smooth edges that drop to zero and when $\beta = 20$ in (c) the edges becomes steeper and the intensity profile at this point approximates uniformity. When β increases beyond $\beta > 20$ the $1D$ intensity profile becomes flatter with much more sharper edges that approximate the ideal flattop beam.

Figure 1.2 (c) illustrates the evolution of the approximated flattop beam from having a central intensity maximum as a Gaussian beam, to a Super-Gaussian beam with smooth edges and a semi uniform intensity profile and finally an approximated flattop beam with a uniform intensity profile. The beam can be generated in a Cartesian geometry as well, this is done by replacing the radial coordinate into Cartesian coordinates $\left(r = \sqrt{x^2 + y^2 + z^2}\right)$.

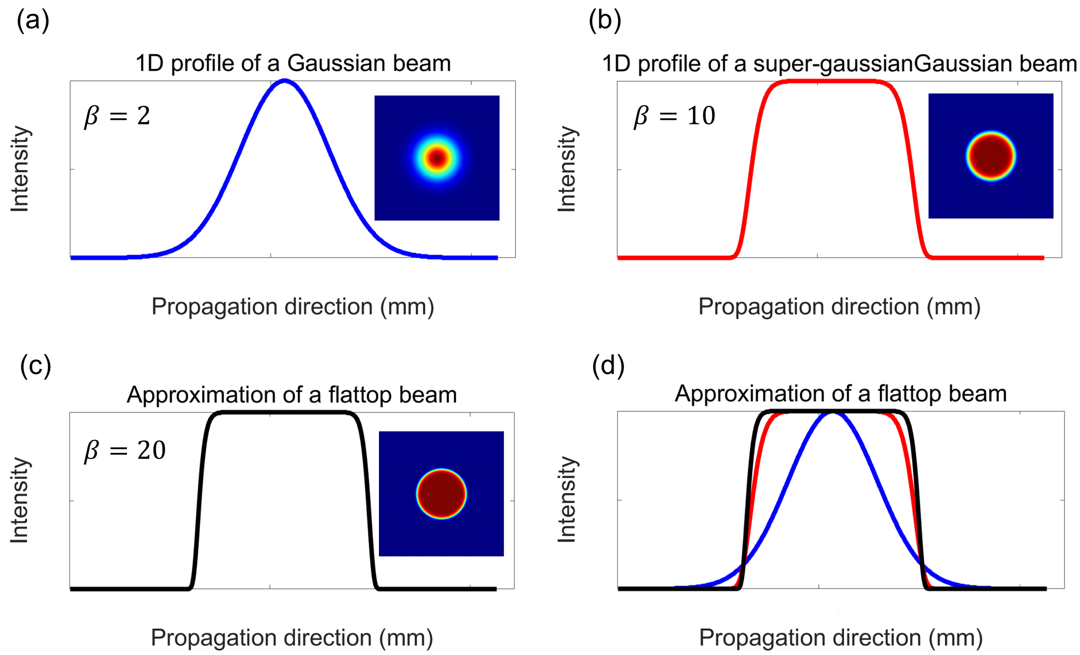

FIGURE 1.2: Approximation of the flattop beam by controlling β to obtain $1D$ intensity profile. $\beta = 2$, we have a bell-shaped Gaussian intensity profile labeled (a), when $\beta = 10$ we have a super-Gaussian mode with smooth edges labeled (b), and when $\beta = 20$ the edges become steeper representing an ideal flattop beam labeled (c). The graph labeled (d) is a simulation of three different modes already discussed in (a), (b) and (c) all on the same axes.

Chapter 2

Devices to create structured light

2.1 Overview of liquid crystal on silicon spatial light modulators

The ability to shape light is believed to date back as early as 212 BC when the Greek scientist Archimedes used many mirrors to set an invading Roman ship on fire [88]–[90]. The mirrors were used to focus the radiation coming from the sun to a spot size which can cause flames due to its concentrated spatial frequency. Monochromatic beam shaping had to wait until 1960, when a physicist Theodore Maiman discovered the first laser generated through a ruby crystal pump [91]. Fred Dicky reports from [92] the footprint of beam shaping after the discovery of the first laser. The first paper published on beam shaping was in 1965, in his work, Freiden used a field mapping technique [92]–[94] made of two plano-aspheric telescope system to convert a plane wave into a beam with a uniform intensity (flattop beam) [95].

It took 9 years for Olof Bryngdahl to publish 2 papers on map transformations by using a CGH on a phase filter imaged with 2 lenses, the first lens was responsible for Fourier transforming an arbitrary hologram on a phase filter while the second lens is responsible to re-collimate the flattop beam to maintain the phase distribution [96], [97]. Today we still make use of conventional techniques to shape light, however, we use a more dynamic technology that is fabricated to shape light through a holographic approach, this is a micro-display LCoS-SLM. Unlike the conventional refractive beam shaping techniques already explained above, LCoS-SLMs are not just limited to beams with a uniform intensity profile but they are also able to shape other intensity structures [98].

Phase only LCoS-SLM devices makes use of two technologies: the first are the twisted nematic LC molecules which are in between the crystals and liquid states of matter [99] and are used to alter the polarisation state of an incident beam due to their birefringence property given by

$$\sigma_n = \sigma_e - \sigma_0, \tag{2.1}$$

where σ_0 and σ_e are the refractive index of the ordinary and the extraordinary indexes for incident light polarised perpendicular and parallel to the director of the LC molecules respectively [100]. The second property is what makes the device reflective, each pixel is made up of a highly performing reflective silicon complementary oxide semiconductor (CMOS), which has long been implemented for video display applications. The backplane of the CMOS is made up of an electronic circuit which allows the voltage to be applied across each pixels giving rise to an "on state" of the device. The on state simply means the LCs rotate resulting in the change of their refractive index which affects the phase delay [101] of the incident light reflected off the LCD in accordance with equation 2.1. Unlike their competitor, MEMS based DMDs, which are able to modulate any light with different wavelengths [102], LCoS-SLMs have to be calibrated for different wavelengths to achieve a full 0 to 2π phase-shift modulation.

Even though LCoS-SLMs might appear to be a better choice in terms of resolution than other SLMs that are commercially available, they have some few undesirable disadvantages. They are polarisation insensitive and only modulate linearly polarised light. Another disadvantage is that more time is consumed by calibrating the device for a specific laser beam wavelength used in the experiment. LCoS-SLMs also suffer from optical phase delay or phase response time, although high precision holographic image display can still be achieved, a quick phase response time is highly demanded in applications such as optical communication. A phase response time is defined as the time taken for a circuit to change its state by a specified fraction of its total response when subjected to a change in input signal. A LCoS-SLM has a 60 Hz refresh rate [103] as compared to that of a MEMS based DMDs or deformable mirrors which has up to tens of KHz refresh rate [104], [105]. Although it has more drawbacks than the MEMS based DMD, it compensates it for high resolution outputs.

2.2 Spatial Light Modulator

2.2.1 Mechanism

In our lab, we use a HOLOEYE LCoS-SLM to structure light. The mechanical structure is divided into three components as shown in figure 2.1 which are: the control electronic board with video interface HDMI, a flex cable and a pixelated LCD, each of these components has a specific function that leads to both phase manipulation of a laser beam illuminated on the LCD.

As already discussed, LCoS-SLMs work on electrically controlled birefringence to control the polarisation of an incident light as the LCs rotate about their axis as a result of an applied voltage in the control electronic board. In addition to the HDMI port, the control electronic board also has a USB port that connects to the computer and its main purpose is to digitally alter the voltages required to rotate the LCs to achieve a 2π phase modulation of an incident plane wave of a specific wavelength through a calibration procedure (see section 2.2.2). The flex cable is designed to connect the control electronic board to the LCD which in the presence of the applied voltage, the pixels contained in the LCD will then apply a phase retardance on the optical phase of an incident plane wave [106].

The amazing feature about the new Pluto-2.1 version is that it comes with a temperature sensor that is accessible in the configuration manager software. The temperature is always displayed in three colors (green, orange and red). When the temperature is displayed in green it is always for the values between $10°C$ and $55°C$, orange for values between $55°C$ and $65°C$ and red for any value above $65°C$. It is advisable to keep the external temperature slightly below the room temperature, about $23°C$, either to avoid the LCs to heat up and form liquid phase (at high temperature) or solid state (at low temperature) rather than the desired nematic phase.

FIGURE 2.1: A representation of a Pluto-2.1 Holoeye LCoS-SLM with a full HD resolution (1920×1080) where each pixel has a pitch of 8 μm. The device is made up of three components, a control electronic board, a flex cable and a LCD [107]

2.2.2 Calibration

Before the device can be calibrated, the laser beam has to be aligned so that it propagates parallel with the optical table. The laser beam is aligned with two mirrors, ($M1$ and $M2$) and two apertures, $A1$ and $A2$ as shown in figure 2.2. Calibration is conducted by carefully varying the voltage(s) of the SLM to achieve a phase-shift from 0 to 2π in each pixel of the LCD screen. A change in the voltage changes the rotation of the LCs in each pixel which in turn alters the polarisation state of the incident light as it reflects off of the LCD screen. Figure 2.3 shows the alignment of the LCs contained in each pixel of the LCD. The figure also illustrates that the LCs always orientates in the direction of the electric field as a result of the induced voltage(s).

Figure 2.4 illustrates an experimental setup used to calibrate the LCoS-SLM for a helium neon (HeNe) laser with wavelength ($\lambda \approx 633$ nm). Here, two lenses L_1 (25.4 mm)»L_2(300 mm) are placed exactly $L_1 + L_2$ apart in front of a laser source emitting a Gaussian laser beam. The first lens (L_1) is used to expand the beam along the propagation direction (z), while the second lens L_2 is used to collimate the beam to maintain the same beam waist (ω_0 as it propagates). The reason for expanding and collimating the laser beam is to overfill the LCD with a plane wavefront. When this plane wavefront passes through a two pinhole mask, it creates two identical plane waves which are incident and centered onto the LCD. The two plane waves are reflected off the LCD and they overlap/interfere at the focal plane of the third lens (fourier plane) $L_3 = 150$ mm, fringes like the ones seen at the bottom of figure 2.4 will be formed at the focal plane of the lens L_3.

The fringes are mathematically described by the following equations:

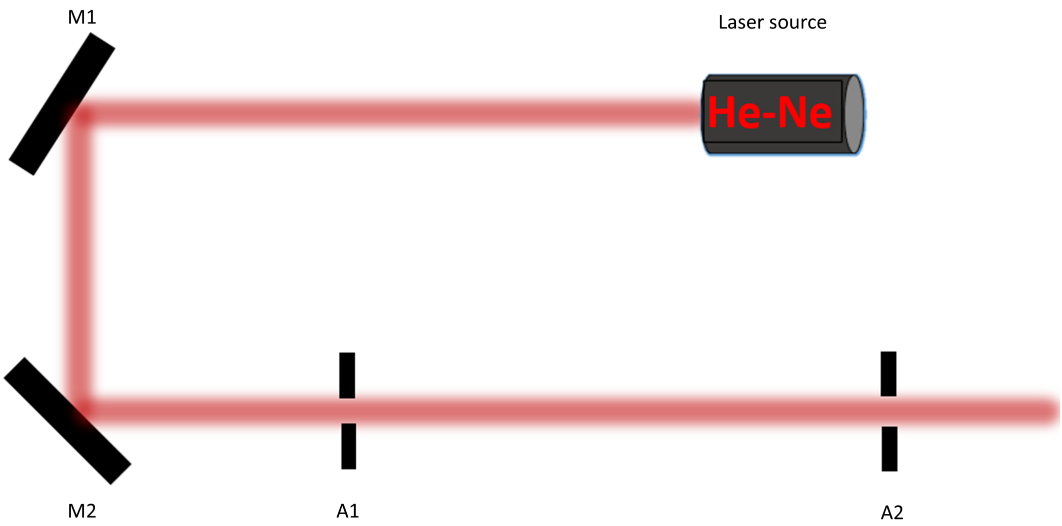

FIGURE 2.2: An experimental laser beam alignment setup before the SLM calibration. Two mirrors $M1$ and $M2$ are used to make sure that the incoming laser beam from the laser beam source pass through the centers of each aperture $A1$ and $A2$.

$$u_1 \approx \exp\left(i\Phi_1\right), \tag{2.2}$$

$$u_2 \approx \exp\left(i\Phi_2\right), \tag{2.3}$$

where u_1 and u_2 are the electric fields of the two plane waves. Since the two plane waves overlap with one another, it is clear that the two fields have to be added together to obtain the total intensity profile of the interference pattern given by the absolute squared of the sum of the two fields which takes the following expression:

$$I_{out} \approx |u_1 + u_2|^2, \tag{2.4}$$

From figure 2.4, it is seen that the interference pattern causes a phase-shift from 0 to 2π throughout all 256 grey levels. A phase-shift is a binary region, where 0 represents no phase-shift at a dark region, and 2π indicates a phase-shift at the bright region. Only one plane wave goes through a phase-shift from 0 to 2π while the other plane wave remains at 0. The plane wave (u_1) maintains a fixed phase-shift (0), while the other plane wave (u_2) undergoes a phase-shift (from 0 to 2π) with the following expression:

$$u_2 \approx \exp\left(i(\Phi_2 + \delta)\right), \tag{2.5}$$

where δ is the phase-shift component affecting the second electric field (u_2). The intensity profile of the interference profile as one beam undergoes a phase-shift is given by:

$$I_{out} = |u_1 + u_2|^2. \tag{2.6}$$

In plot (a) in figure 2.5, there is a deviation between the measured and the desired phase-shift. This is because the SLM has not been properly calibrated for the desired laser beam wavelength. This was rectified in plot (b) by adjusting the voltage that addresses each individual pixel until we successfully achieve a desired 2π phase-shift.

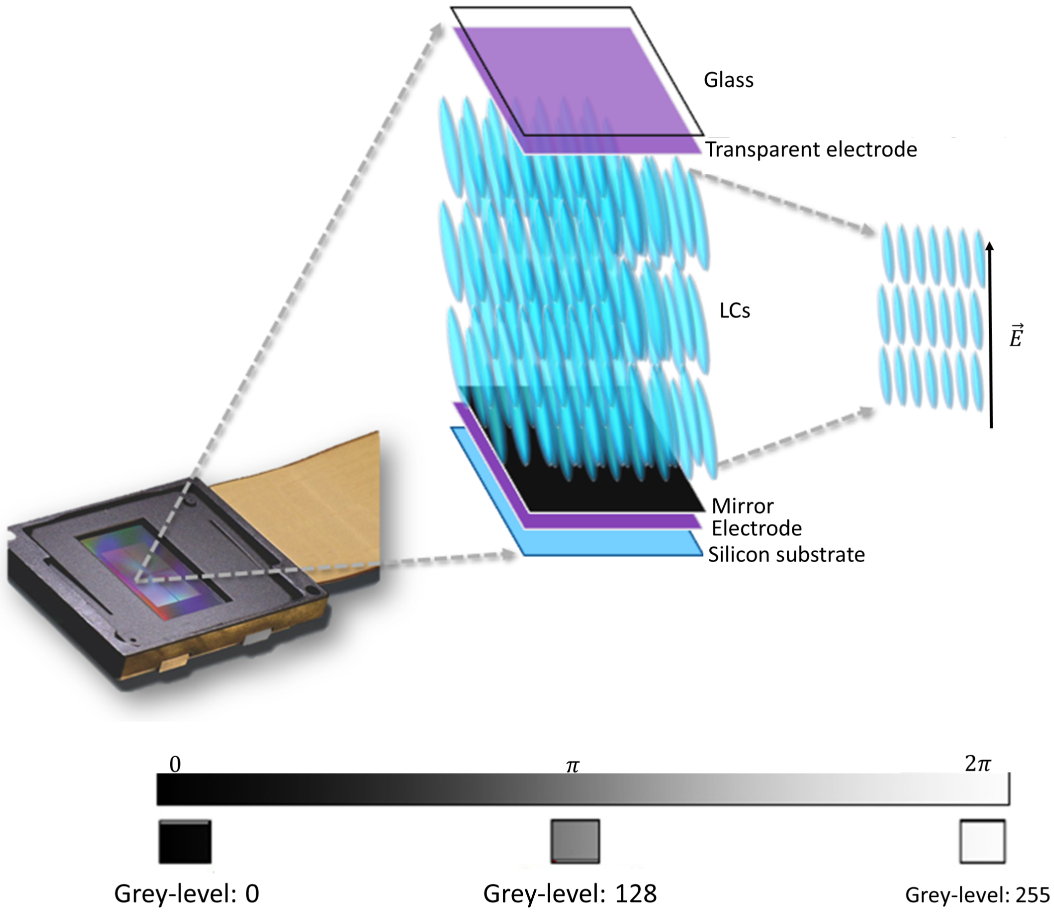

FIGURE 2.3: A schematic representation of how the induced electric field changes the rotation of the LCs. The LC rotation changes the phase of the incident light and as a result, there is a phase-shift that occurs from 0 to 2π across all 256 grey-scale. Adapted from [107]

2.2.3 SLM characterisation

Diffraction grating measurements

Beam splitting is a phenomenon that occurs in everyday life, this is when light splits into various beamlets, each containing the information and power distribution from the incident beam they were divided from [108]. A good example of a beam splitting occurrence we see almost every time after it rains is the rainbow displaying numerous colors due to a spectrum of wavelength division known as spectral beam splitting [109], however this is a refraction occurrence where white light splits into different wavelengths of light. In this study we will investigate the effects of a beam splitting through a diffraction grating with a monochromatic beam.

A diffraction grating is a $2D$ DOE made of slits or surface relief patterns used to divide or disperse light into different diffractive orders based on the wavelength in study [110], [111]. In the case of a polychromatic light (white light), different color patterns will appear on the screen depending on their wavelength spectrum as light passes through the diffraction grating.

In our lab we use holographic gratings to spatially separate the desired 1^{st} order

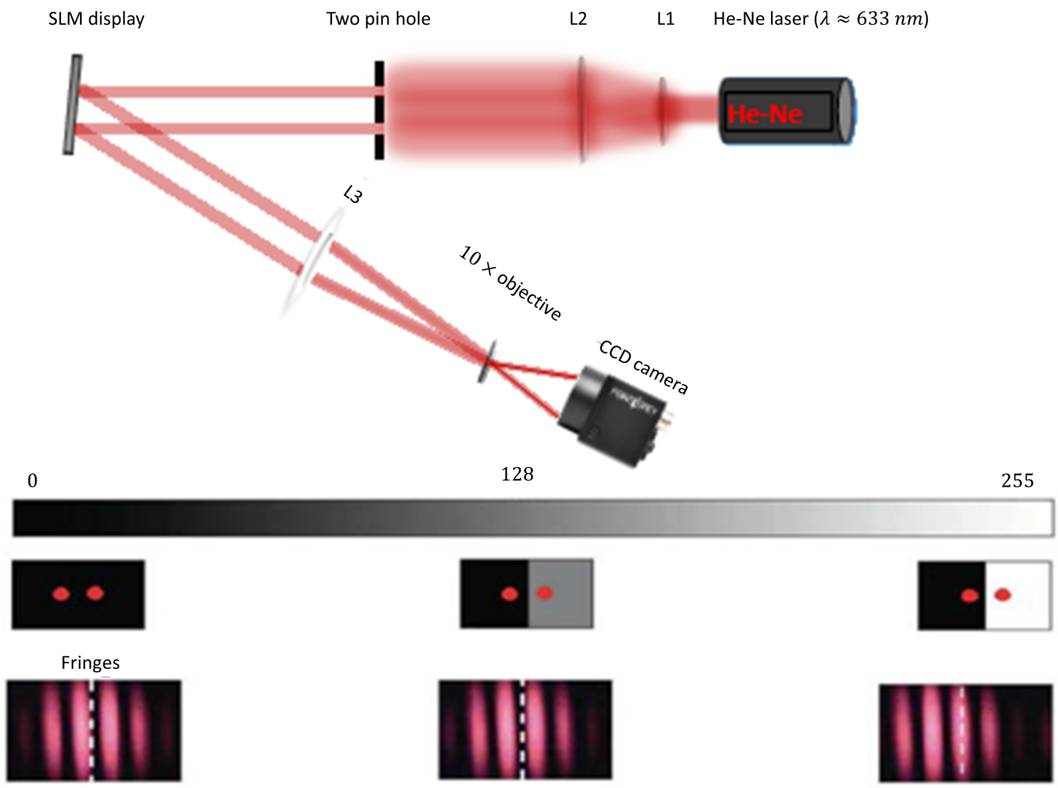

FIGURE 2.4: An experimental setup used for calibrating the SLM to achieve a 2π phaseshift

away from the 0^{th} unmodulated order. Amongst the holographic grating we have the sinusoidal holographic grating and the blazed holographic grating. A sinusoidal grating is made up of symmetrical long, narrow channels or grooves that assumes a sine wave function. The transformation of a sinusoidal grating into a sawtooth function is known as a blazed holographic grating, and this type of grating is preferred because unlike the sinusoidal grating which offers about 40% in the 1^{st} order, it is able to transfer close to a 100% efficiency from the 0^{th} order into the 1^{st} desired order.

Even though the sinusoidal grating is not as efficient as the blazed grating, we want to examine how the spacing between the slits or grooves affect the spacing between the 1^{st} desired order and the 0^{th} order. The lines seen on the hologram in figure 2.6 represents the grating slits and the spacing between the slits is defined by a variable d. Since we are using a CGH, the grating function is added onto the phase of the modulated beam, and the full hologram expression imparted onto the LCD is given by

$$\Psi_{LCD} = f(A(r)) \sin\left(\Phi(r,z) + (G_x x + G_y y)\right), \tag{2.7}$$

where the parameters:

$$G_x = \frac{n_x}{(x_{pixels})\,(8 \times 10^{-8} m)}, G_y = \frac{n_y}{(y_{pixels})\,(8 \times 10^{-8} m)} \tag{2.8}$$

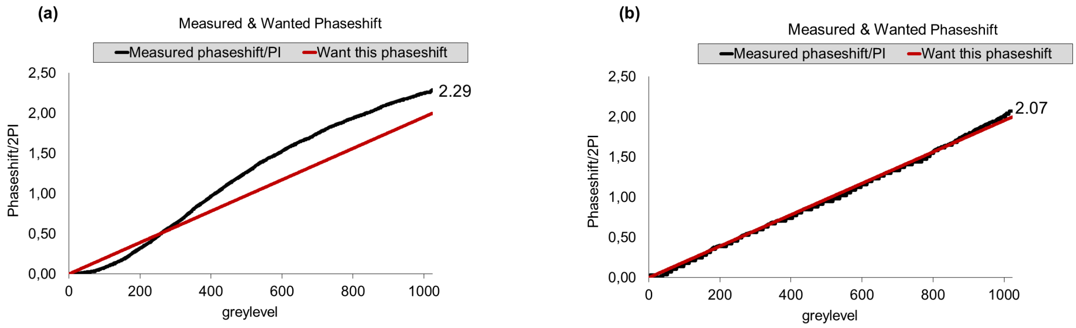

FIGURE 2.5: Phaseshift vs gray-level plot of the measured and wanted phaseshifts. Plot (a) illustrates the desired phase-shift (red curve) before calibration and plot (b) illustrates the phase-shift after calibration process (black curve)

are the grating periods in the x and y directions respectively, n_x and n_y are positive integers, and $f(A(r))$ is the amplitude phase term. The variables x_{pixels} and y_{pixels} in equation 2.8 represents the LCD screen dimensions in pixels, which are 1920 and 1080 respectively. We only controlled the grating period along the x-plane and set $(n_y = 0)$ for a better visualisation along the x-axis. As we increase the grating frequency (from 4 pixels) the spacing between the lines increases as the number of lines decreases. As a result the separation (Y) between the 0^{th} and 1^{st} order decreases. To calculate the distance between the 0^{th} and the 1^{st} order we used the grating equation, and then calculated the diffraction angle (θ). The grating equation is given by [110]:

$$d \sin(\theta) = m\lambda, \tag{2.9}$$

where d is the spacing between the slits and m is the order number, and since we desire the 1^{st} order, $(m = 1)$. Now to calculate Y we use a tan function

$$Y = D \tan(\theta), \tag{2.10}$$

where D is the distance between the LCD and the region where the diffraction orders appear. By making θ in equation 2.9 the subject of the formula and substituting it into 2.10, we obtain:

$$Y = D \tan\left[\sin^{-1}\left(\frac{m\lambda}{d}\right)\right]. \tag{2.11}$$

The results were obtained by encoding 9 different grating frequencies from 4 to 20 pixels in steps of 2 pixels. The number of lines like the ones seen in the hologram of figure 2.6 are obtained in the following equation,

$$d = \frac{S}{n_{lines}}, \tag{2.12}$$

where n_{lines} is the number of lines seen in the hologram figure 2.6 and S is the size of the LCD. Figure 2.6 plays a huge role in beam shaping because understanding how a diffraction grating works is the fundamental key to beam shaping. The spacing between the lines in figure 2.6 (b) are represented by (d) in (b). The number of lines (n_{lines}) are controlled by the grating frequency. The distance between the 1^{st} order and the 0^{th} order were measured using a vernier caliper. Figure 2.7 illustrates the effects of the sinusoidal grating on the orders of diffraction (1^{st} and 0^{th} order). We calculated Y between the 0^{th} and the 1^{st} order using equation 2.50. We then saw that an increase in the grating frequency results in the decrease in the spacing between the orders. The error bars seen in the plot were calculated using the standard error method, this is obtained by dividing the standard deviation of the data set (Y) by the square root of the number of data points. This is expressed using the following equation,

$$SE = \frac{\sigma}{\sqrt{n}}. \tag{2.13}$$

In equation 2.13 SE is the standard error, σ is the standard deviation and n is the sample number.

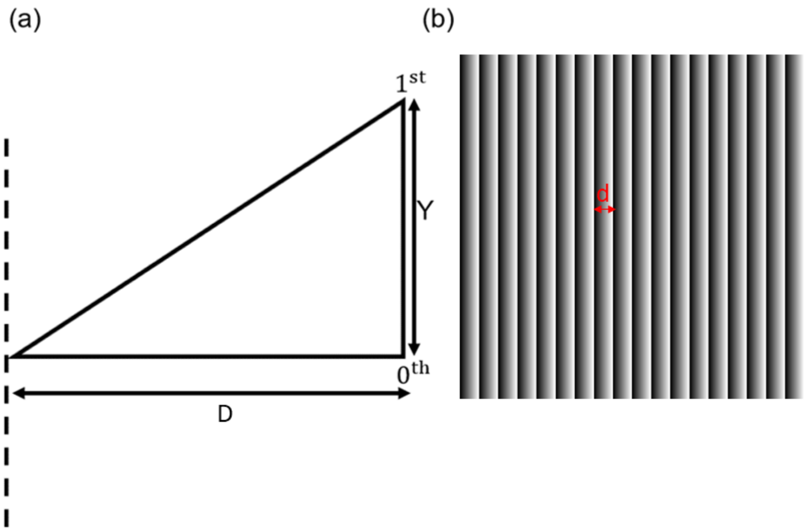

FIGURE 2.6: Diagram (a) shows the effects of grating on the distance (Y) between the 0^{th} and the 1^{st} order. Where D is the distance between the LCD and the point where the diffraction orders appear. The hologram (b) shows the effects of the grating frequency on the pitch (d) as the lines displayed on the grating hologram increase or decrease depending on the grating frequency(s).

2.2.4 Efficiency measurements

Since LCDs are pixelated, when the laser beam is reflected off of the LCD it separates into many orders of diffraction. Amongst those orders, there is an unmodulated 0^{th} order reference beam that consumes most of the transverse intensity profile of the beam. We add a diffraction grating function to separate the 0^{th} order from the desired 1^{st} order and thereafter we use an aperture to allow only the 1^{st} order through, while filtering out all other orders. The full hologram expression with both the phase and the diffraction grating is expressed as:

$$\Psi_{LCD} = \text{mod}\left[\Phi(r,z) + 2\pi\left(x\frac{G_x}{\lambda f} + y\frac{G_y}{\lambda f}\right), 2\pi\right], \tag{2.14}$$

where $\Phi(r,z)$ is the phase of a spatial mode in the transverse direction. Assuming that in equation 2.14, a lens with a focal length f is placed f distance away from the LCD which is intended to separate the 1^{st} order mode away from the 0^{th} order and other higher order modes. The coordinates $G_x = g_x\lambda f$ and $G_y = g_y\lambda f$ are related to the grating frequencies (g_x and g_y) and the lens of a certain focal length [112]. If

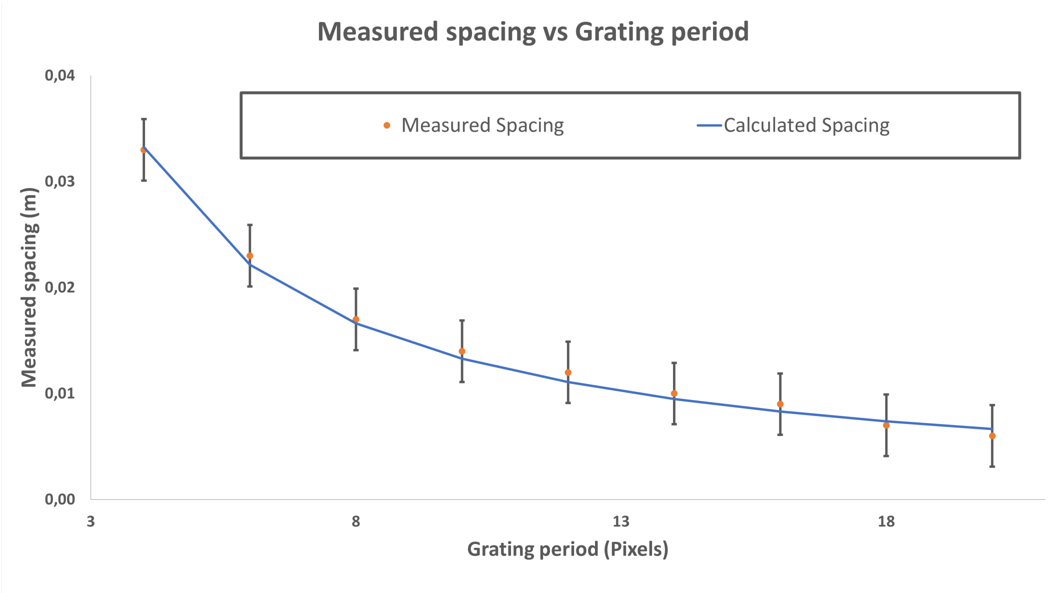

FIGURE 2.7: Effects of diffraction grating on the spacing between the zeroth and first order

we set $G_y y = 0$ and vary $G_x x$, the orders will disperse along the x direction and vise versa. If both frequencies are varied, the orders will disperse in the diagonal direction.

There are three (type 1, type 2 and type 3) different encoding techniques compiled by Victor Arrizon et al [113]. Type 1. since we lose efficiency from the pixelated modulator, we tested which technique produced the best efficiency or power output. To begin, Arrizon et al proposed a complex field given by:

$$u(x,y) = a(x,y)\exp\left(i\Phi(x,y)\right), \tag{2.15}$$

where x and y are just spatial coordinates and $\Phi(x,y)$ represents any arbitrary phase profile. Both amplitude and phase terms assumes [0,1] and [-π,π] respectively. The main aim is to encode the complex field in terms of the phase transmittance CGH function given by:

$$T(x,y) = \exp\left(i\psi(a,\Phi)\right), \tag{2.16}$$

where the CGH $\psi\left(\Phi,a\right)$ is the function of the amplitude $a(x,y)$ and the phase $\left(\Phi\left(x,y\right)\right)$ of a desired field. Below is a set of equations to write the transmission function as a Fourier series in the domain Φ. Consider a transmission function in equation 2.16 rewritten as:

$$\frac{iq}{\phi} = \sum_{q=-\infty}^{\infty} C_{(a,n)}\exp\left(in\Phi\right). \tag{2.17}$$

In equation 2.17, q is the qth order mode investigated, ϕ is the phase of the generated beam profile and $C_{(a,n)}$ is the qth order coefficient when $n = q$. Multiplying both sides by $e^{-in\Phi}$ and integrating both sides from -π to π we obtain:

$$\int_{-\pi}^{\pi} T\left(x,y\right)\exp\left(-in\Phi\right)d\Phi = \sum_{q=-\infty}^{\infty} C_{a,q}\int_{-\pi}^{\pi}\exp\left(i\left(q-n\right)\Phi\right)d\Phi, \tag{2.18}$$

If we use Euler's formula on the right hand side of equation 2.18 we obtain:

$$\int_{-\pi}^{\pi}\exp\left(i\left(q-n\right)\Phi\right)d\Phi = \int_{-\pi}^{\pi} cos\left(q-n\right)\Phi d\Phi + i\int_{-\pi}^{\pi} sin\left(q-n\right)\Phi d\Phi. \tag{2.19}$$

Equation 2.19 is equal to 2π if $q = n$ and 0 if $q \neq n$. Rewriting 2.18, we achieve the following equation:

$$\int_{-\pi}^{\pi}\exp\left(i\psi\left(a,\Phi\right)\right)\exp\left(-in\Phi\right)d\Phi = C_{a,n}2\pi, \tag{2.20}$$

which leads to the coefficient Fourier transform that takes the form:

$$C_{a,n} = \frac{1}{2\pi}\int_{-\pi}^{\pi}\exp\left(i\psi\left(a,\Phi\right)\right)\exp\left(-in\Phi\right)d\Phi. \tag{2.21}$$

Equation 2.21 can also take the form of Euler's equation,

$$C_{a,n} = \frac{1}{2\pi}\left[\int_{-\pi}^{\pi} cos\left(\psi(a,\Phi) - n\Phi\right)d\Phi + i\int_{-\pi}^{\pi} sin\left(\psi\left(a,\Phi\right) - n\Phi\right)d\Phi\right]. \tag{2.22}$$

Since after integrating Φ in equation 2.21, the coefficients $C_{a,n}$ are still dependent on amplitude (a). The complex field signal in equation 2.15 is recovered by choosing the first order $(n = 1)$ in equation 2.21. The signal encoding condition

$$C_{a,1} = Ka, \tag{2.23}$$

is satisfied when K is a positive constant $(K \geq 1)$. We further outline the necessary conditions to satisfy equation 2.23, which are

$$\int_{-\pi}^{\pi}\sin\left[\Psi(\Phi,a) - \Phi\right]d\Phi = 0, \tag{2.24}$$

$$\int_{-\pi}^{\pi}\cos\left[\Psi(\Phi,a) - \Phi\right]d\Phi = 2\pi Ka, \tag{2.25}$$

we can thus determine suitable CGHs from equation 2.24 and equation 2.25. To test the efficiency of three encoding techniques, we first measure the input power (P_{in}) of the expanded and collimated plane wave that is illuminated on the LCD, which is 10.9 mW, this will serve as a total power from which the diffracted orders are generated from. Instead of encoding LG beams just like how Arrizon et al. did, we encoded a Gaussian beam. We were interested to investigate the most efficient technique to use for beam shaping. Figure 2.8 below shows the experimental setup used to measure the power of the 0^{th} order in table 2.1 and the power of the 1^{st} order in table 2.2 for all three encoding techniques. All measurements were taken in the far-field. The efficiency is achieved by calculating the ratio between P_{out} and P_{in} in percentage (Efficiency $(\%) = \frac{P_{out}}{P_{in}} \times 100\%$) as shown in table 2.1 and table 2.2.

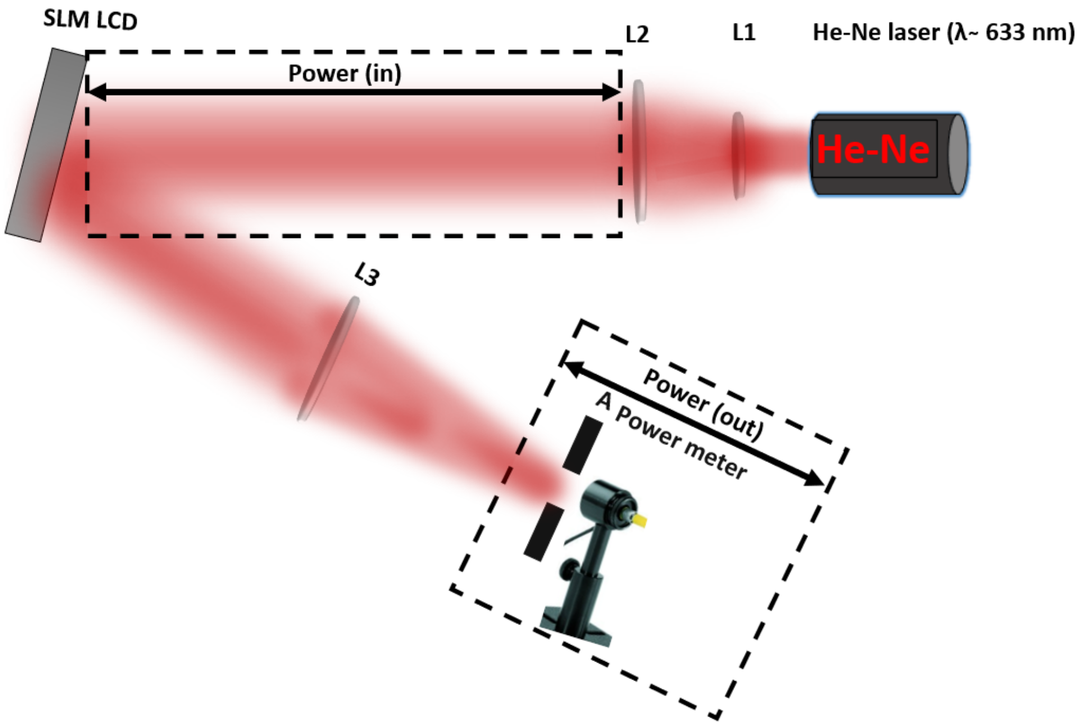

FIGURE 2.8: Experimental setup to measure input power of an expanded and collimated beam. The beam is expanded and collimated using a telescope ($L_1 = 25.5\ mm$ and $L_2 = 300\ mm$). The power output was measured in the far-field using lens ($L_3 = 150mm$).

Technique	P_{in}	P_{out}	Efficiency (%)
Type 1	10.9 mW	7.93 mW	68.80%
Type 2	10.9 mW	7.40 mW	67.88%
Type 3	10.9 mW	7.50 mW	70.64%

TABLE 2.1: The 0^{th} order output efficiencies for the three encoding techniques.

The power meter we used in table 2.1 had a smallest measurable value of 0.1 Mw which is taken as the error in the experimental measurements. From table 2.1, we see that about 30% of the power in all the encoding techniques is dissipated in other orders of diffraction. From table 2.1, we can already predict that type 3 enconding technique will produce the lowest efficiency amongst the three, and if we refer to table 2.2, type 1 and type 2 appear to produce more efficiency than type 3.

2.2.5 Generated spatial modes

Now that the calibration and characterization of the LCoS-SLM is complete, we can move to some generated spatial modes. Consider a phase only vortex beam given by equation 1.68 with a $\ell = 3$ as illustrated in figure 2.9. The hologram displayed on the right is the product of the phase in equation 1.68 and a grating represented by the phase ramp which forms a fork-like hologram with the first order intensity profile that has a null central intensity profile.

Technique	P_{in}	P_{out}	Efficiency (%)
Type 1	10.9 mW	0.3 mW	2.75%
Type 2	10.9 mW	0.3 mW	2.75%
Type 3	10.9 mW	0.2 mW	1.80%

TABLE 2.2: The 1^{st} order output efficiencies for the three encoding techniques.

Bereneice et al., studied the scalar vortex beam which is not a solution to the paraxial wave equation, although when the radial mode $(p = 0)$ is disregarded, there are some unwanted rings around the core vortex intensity profile that cannot be controlled or removed. The radial modes seen around a vortex beam manifest as result of radial indices when they are analysed in terms of the LG modes [114]. This can be rectified with a complex modulation, by adding an amplitude term in equation 1.68 to generate an LG beam ($LG_{\ell,p}$) given by:

$$A = \left(\frac{\sqrt{2}\rho}{\omega(z)}\right)^{|\ell|} \exp\left(-\left(\frac{\rho}{\omega z}\right)^2\right) lg_p^{|\ell|}\left(\frac{2\rho^2}{\omega^2(z)}\right) \exp\left[\left(\frac{ik\rho^2}{2R(z)}\right)\right] \exp\left[i\psi(p,\ell,z)\right]. \tag{2.26}$$

Through the complex beam modulation, we are able to control the number of rings we desire around the core vortex beam. Figure 2.10, shows some generated LG beams by demonstrating the effect the radial and topological modes have on the generated beam. As the radial mode (p) increases from left to right while keeping $\ell = 0$, we obtain a maximum of 3 rings from $(p = 1, p = 2$ and $p = 3)$ around a central maxima Gaussian beam. We have already gone through the effects of the topological charge on the plane wave which introduces a twist to the converted plane wave. In figure 2.10, we see how the vortex beam increases in diameter as ℓ increases from top to bottom. This means the wavefront makes a large twist with increasing ℓ. If we set $\ell = 0$ and $p = 0$, we return to the fundamental Gaussian beam with an electric field described in equation 1.31.

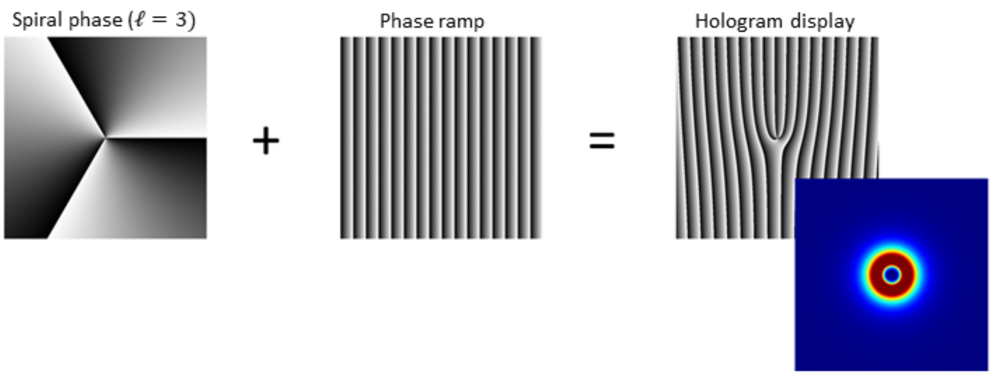

FIGURE 2.9: Generation of a vortex beam carrying a well defined OAM which is imparted on the LCD. The phase has to be added to the phase ramp to separate the 1^{st} order from the undiffracted 0^{th} order. The insert on the right is the intensity profile of the vortex mode.

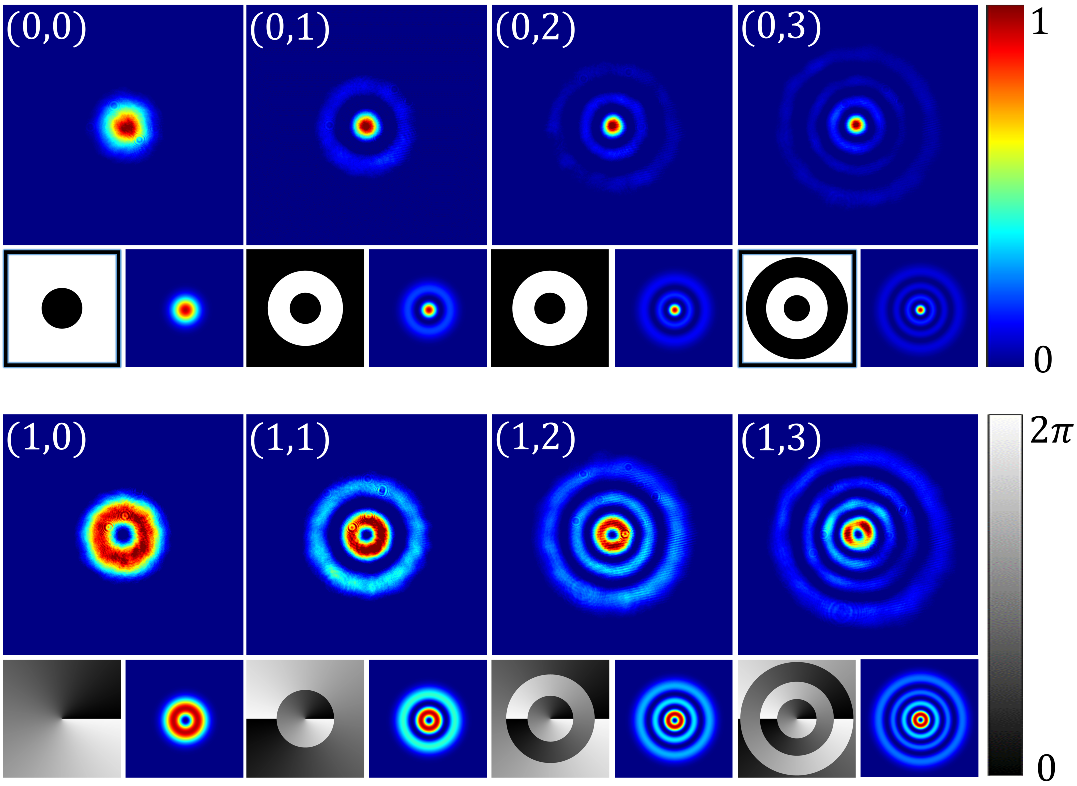

FIGURE 2.10: The effects of the ℓ, and p indices on the LG beams propagating along the propagation axis in free-space. The experimental modes are on top of each row with the simulated counterparts at the bottom right with their respective phase profiles on the bottom left of each ℓ and p. Topological charge ℓ increases from top to bottom and the radial mode (p) increases from left to right. The phase profiles were simulated without a grating functions for a clear visualisation of the phase profiles.

2.2.6 Figures of merit

A Figure of merit (FoM) is a term used to quantify the generated spatial modes to evaluate how close they are to the simulated theoretical counterpart. There are different ways to verify the quality or purity of the generated beam(s). We can either measure the efficiency of the 1^{st} order of the beam detected by the CCD camera sensor, however, efficiency alone is not the most reliable factor to quantify a measurement because we can obtain a high efficient beam that is highly abberated. We then introduce another factor known as "correlation", and this is used to compare how well the measured data fits or agrees with the theoretical or desired data counterpart, this can be used alone if efficiency of the generated beam is not that much of a concern or if we want to evaluate how well a modulator can generate a desired beam(s). In the case where efficiency is required for example in laser material processing applications, we make use of both the efficiency and the correlation to quantify the generated beam in the desired plane of interest. FoM in this case is mathematically expressed as:

$$FoM = \frac{\sum \left(I_D - I_D'\right)\left(I_E - I_E'\right)}{\sqrt{\sum \left(I_D - I_D'\right)^2 \sum \left(I_E - I_E'\right)^2}} \times \frac{\sum \left(I_E'\right)}{\sum \left(I_D\right)}, \tag{2.27}$$

where I_D is the desired intensity profile, I_E is the experimental intensity profile taken at the region of interest, the total sum over all coordinates is represented by $\sum$, $I_D^{'}$ and $I_E^{'}$ are the average intensities of the desired and experimental intensities respectively. In equation 2.27 the first term describes the correlation between the experimental and the desired intensity profiles, while the second term describes intensity efficiency of the experimental intensity profile in the region of interest. To achieve a high beam purity with good beam efficiency, FoM must be high.

In figure 2.11 we made use of the correlation method alone to analyse the purity of the LG beams generated. If we take an example in figure 2.10 of $LG_{(1,2)}$ as shown in figure 2.11 (with (a) being the measured beam and (b) being the theoretical beam), we see that the measured beam agrees well with the theoretical beam with a correlation measurement of 0.84. In the case of analysing both the efficiency and the correlation we use a Cartesian flattop beam as an example, since a uniform intensity beam profile is used in laser processing applications and so the beam purity together with the efficiency has to be high.

Figure 2.12 shows the beam purity of the experimental cartesian flattop beam (a) and the theoretical counterpart in (b) with a correlation value of 0.99 and the efficiency value of 0.92 resulting from a blazed grating, using equation 2.27, we obtain a $FoM = 0.92$, which is very high and shows that the modulator is able to generate high FoM spatial profiles.

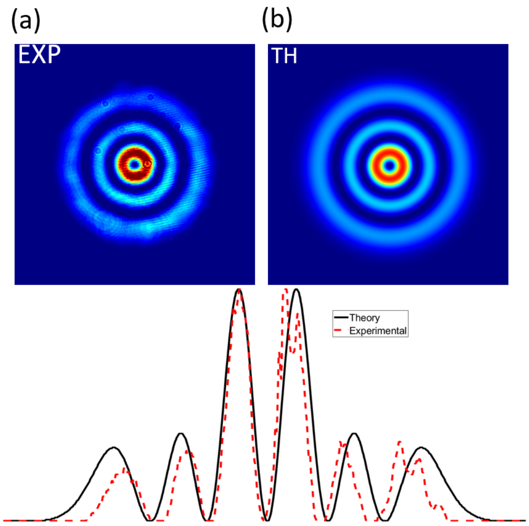

FIGURE 2.11: Correlation between the experimental LG beam and theoretical counterpart with $\ell = 1$ and $p = 2$, which showed a 0.84 correlation. This shows a good beam purity of the experimental beam which agrees well with the theory.

2.3 Deformable Mirrors

At first adaptive optics with deformable mirrors was introduced for astronomical purposes so that scientists could see past the clouds and broaden the various spectrum in space which includes the moon and stars. With this great opportunity, comes a great obstacle we ought to overcome, which are the atmospheric aberrations (turbulence) [115]. The effects of atmospheric turbulence on light is a phenomenon that

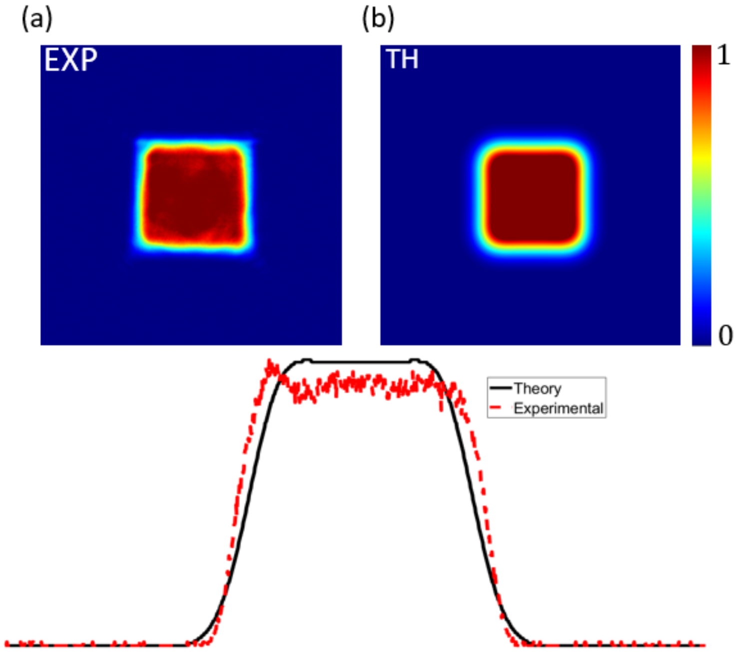

FIGURE 2.12: A quantisation of the experimental cartesian experimental result (a) in reference with its theoretical counterpart (b). The beam purity of the measured result agrees well with the theoretical data.

occurs as a result of both spatial and temporal random variations of the refractive index which causes light to distort as it passes through the Earth's layer. Since there is a change in the refractive index that light is subjected to, this means that light changes both the propagation direction and its spatial intensity profile, the rapid change in the affected intensity profile is known as scintillation [116]–[119].

Atmospheric turbulence is an issue in beam shaping for applications like free-space optical communication where the beam propagates outside the fibre, in free-space and as a result of change in temperature and pressure fluctuations in the atmosphere this leads to random change in refractive index which distorts the phase and amplitude of the beam [120]. Suppose we create a communication system between Alice and Bob, where Alice transmits signals in free-space to the receiver, Bob, due to the fluctuations of the amplitude and phase of the transmitted signals, Bob will never get the message that Alice is trying to deliver. To fix this, a deformable mirror combined with a wavefront sensor and a real-time controller, which work together to compensate for distorted incident wavefronts affected by the atmosphere [12], Bob will now be able to receive and analyse the message delivered by Alice.

The first known deformable mirror dates way back to 1953 when H.W Babcock proposed the concept of adaptive optics with deformable mirrors [121], [122]. He saw that the beam propagating through the atmosphere in a telescope experienced all sorts of aberrations and as a result the images were very blurry. The deformable mirror device was called the eidophor which was fabricated using a reflective mirror coated with a thin layer of oil. With the right amount of voltage induced on the thin layer covered with oil the reflective surface deformed into specific patterns to corrected the blurriness occurrence.

The eidophor deformable mirror can be thought of the one seen in figure 2.13. With the right amount of voltage needed to deform the reflective surface of the mirror. The surface deforms into a conjugate pattern of the distorted wavefront for an optimal wavefront rectification as illustrated from the distorted and corrected wavefronts.

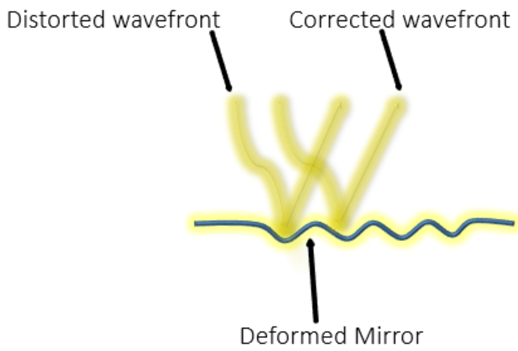

FIGURE 2.13: An illustration of how the surface of a deformable mirror deforms in response to an applied current to compensate the distorted incident wavefronts. The amount of voltage applied is measured by the type of distorted wavefronts it has to rectify.

In the early seventies, the development of the deformable mirrors were based on piezoelectric and electrostrictive materials which had a much quicker response rate, more reliable, and relatively low power comsumption than the eidophor deformable mirror. The most widely used types are the bimorph and segmented piston types [122].

Bimorph deformable mirrors are made up of two poled piezoelectric ceramic wafers with the surface covered with a thin glass sheet which is meant to protect the mirror's metallic coating against all possible damage, for example, dust or light if it's over-exposed [123]. Since the wafers are poled, they experience a piezoelectric effect which is the electric charge stored in response to the mechanical stress induced in the system. The electrodes bonded between the ceramic wafers are responsible to deform the reflective surface by expanding the wafer at one point while the other wafer contracts in response to the applied voltage[124]. When the voltage applied to the wafers has the same polarity as that of the electrodes attached to the wafers, then the surface will experience an expansion and if the applied voltage has an opposite poling as that of the electrode, the wafers will experience a contraction [125]. Since the bimorph deformable mirror is made up of a continuous face-sheet piezoelectric reflective surface, contraction and expansion of the wafers at a controlled voltage must follow a sinusoidal wavelike deformation and sometimes this limits the stroke in the system since the deformation of the wafers depends on the neighbouring electrodes.

Piston deformable mirrors are part of segmented deformable mirrors consisting of mirrors packed close together but controlled individually, this type of device is not deformable but instead the mirror segments are rigid and only go up and down. The mirror segments are controlled by one or more DoFs, where one DoFs represents one actuator attached to a single mirror segment. The advantage about these devices is that unlike the continuous faceplate deformable mirrors, the actuator stroke which is the maximum displacement an actuator can push or pull the mirror segment(s) does not depend on the neighbouring actuator stroke but instead moves independently to compensate for abberated phase distortions of an optical wavefront [126]. The disadvantage of the piston only deformable mirrors is that there are spaces in between the mirror segments, and even more gaps when one segment is pulled or pushed (actuator stroke) which may cause some diffraction loss in an incoming wavefront. This may be a disadvantage for applications that demand a high efficiency laser beam(s) like laser welding and drilling in industrial manufacturing companies. There is a solution to this ordeal and that is to use three DoFs for each mirror segment and that will create a piston tip-tilt configuration which allows less light and diffraction loss [127], this comes at a cost because the more the actuators the more expensive the device is.

Chapter 3

Multi-level DOEs

3.1 Intoduction to DOEs

Rittenhouse reported the first DOE in the seventeen hundreds that could diffract light into many orders, this was a diffraction grating, but this discovery was however unnoticed [128]. In 1821 Fraunhofer brought the idea back to life for spectroscopic applications, which involves the splitting of light into its respective wavelength spectrum [129]. Many invention on diffraction grating appeared henceforth. The first optical element to use diffraction effect is the Fresnel zone plate made of a radially alternating transparent and opaque regions. The work on such a zone plate was published in 1875 by Soret [32], [130]. This device was inefficient since half the power of the diffracted light was absorbed by the opaque region and also half the diffracted light was distributed amongst the generated orders, this left the 1^{st} desired order with less output power.

Lord Rayleigh came up with the solution to increase the efficiency of the zone plate by replacing the opaque region of the zone plate with a uniform and non-absorbing material which would increase the efficiency of the 1^{st} order. Since the zone plate had one half opaque, this means there is a half phase delay with a non absorbing material, with the total amplitude twice as much at the plane of interest and the efficiency in the orders are four times more than with the opaque light absorbing material.

In 1898 Wood designed such a device and published his observations, he also noted that such a device had the potential of generating a 100% efficiency in the desired order by implementing a blazed grating[131]. Tudorovskii approximated a surface relief pattern of a continuous Fresnel phase plate profile counterpart in a discrete stepwise way and considered using a phase plate to correct an optical system from chromatic aberration [132]. Miyamoto took it further and investigated the ability of the phase Fresnel lenses to generate aspheric wavefronts [133].

Rogers discovered the relationship between holograms and Fresnel zone plates [134], he noticed that holograms could produce Fresnel diffraction patterns by using a light source and an arbitrary phase function. In 1972 L.d'Auria et al., proposed a method of fabricating a Fresnel phase microns by using a photolithographic masks technique through a 4-step quantization [135]. Thereafter Clair et al., applied the surface relief profiles on photoresists by controlling the exposure on the photoresist patterns to fabricate a kinoform lens [136]. Even though at that time, holographic optical element technique was a state of the art, it suffered from its inability to produce arbitrary phase functions and it was very difficult to construct and this can be time consuming.

Soon after the invention of holographic optical elements came the proposal of CGHs by Lohmann and Paris in the sixties, they generated binary holograms consisting of dotted patterns on an opaque background [137]. The advantage about CGHs is that any arbitrary phase function can be generated by writing the interference produced by an object wave and a reference wave. They realised that simulating optical holograms first before physical fabrication would save time and money since DOEs can be improved mathematically rather than experimentally. Through CGH technique, phase-only kinoform surface relief diffractive lenses could be fabricated through a step phase lithographic approach. In the beginning of 1980 Veldkamp and Swanson continued from Lohman and Paris and were the first to invent a binary DOE [138].

Binary optical elements makes use of two technologies, namely: a computer-aided design tools and very large scale integration (VLSI) electronic circuit to fabricate surface relief optical devices. The binary devices are formed from high resolute lithographic process (photomasks) to transmit a binerised surface relief pattern onto the optical element. This surface relief pattern is engraved or etched on the optical element by using ion-beam etchers. The term binary comes from the fact that a single etch on the photo resist optical element results in 2-level surface.

In the case where the diffractive surface profiles are not easy to fabricate, an approximation is used in a discrete way, this process involves more than 2-level etching steps, resulting in numerous photolithographic masks, this is referred to as a "multi-level" DOE. Both binary and multi-level DOEs are well suited for lithographic techniques. Multi-level DOEs have a staircase structural property which becomes finer with increasing etching steps, the etching is continuously repeated until an approximation to the continuous element counterpart is achieved.

3.2 Concept to multi-level DOE

This section will illustrate the multi-level experimental procedure used to approximate the smooth "continuous" phase profiles in a discrete fashion. we use the same SLM device already discussed in Chapter 2 to fabricate the multi-level discretized phase-only surface structures. Figure 3.1 (a) and (b) shows the approximation of a smooth linear and phase functions in a discrete multi-level fashion (N steps), with an increment of $N = 2$, $N = 4$, and $N = 8$ respectively as a demonstration of concept. It is clear that the more we increase the steps is the closer we quantize the continuous phase function counterparts.

Implementing a dynamically addressable technology, allows us to investigate the effects of various phase mask geometries and multi-level steps on the resulting intensity profiles. Here, we segment a 2π phase variations for three different types of phase profiles (axicon, cubic and azimuthal) into N-discrete levels and we show that modes of high fidelity can be achieved with only a few phase levels. The multi-level DOEs are achieved by first knowing the function that has to be approximated. Thereafter, the disctretised counterpart is subtracted from the original function, a faster modulate version of itself given by:

$$\Phi_{Multi-level} = \text{mod}(\Phi, 2\pi) - \text{mod}(\Phi, \frac{2\pi}{N}) \tag{3.1}$$

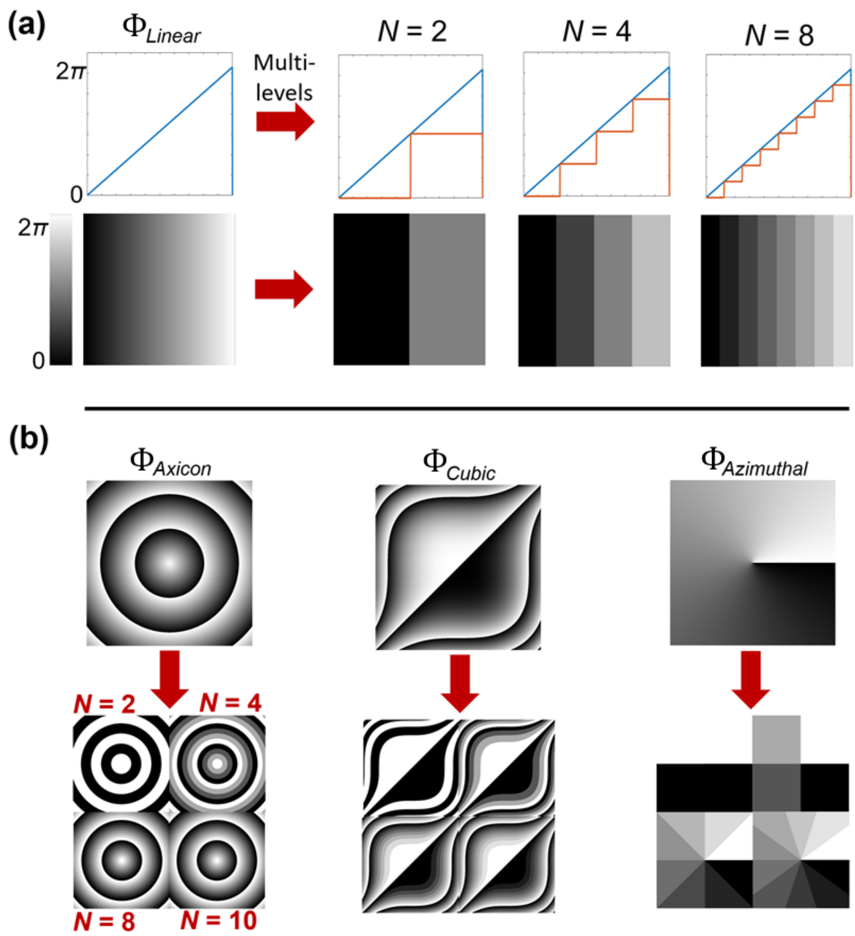

FIGURE 3.1: A 2π modulated multi-level phase, (a) shows a 1 dimensional continuous phase compared with a 1 dimensional discrete multi-level linear phase. The discrete multi-level phase undergoes N phase levels from $N = 2, 4, 8$. As the levels increases we get an approximation of the continuous smooth phase. We used three phase profiles, the axicon, cubic and azimuthal phase to approximate their continuous smooth functions in N multi-levels from $N = 2$ up to $N = 10$ for each phase.

where $0 \neq N \geq 2$. In equation 3.1 $\Phi_{Multi-level}$ is the segmented phase masks that undergoes a series of intensity profile evolution to approximate the continuous phase profile in N discrete phase levels. The number of orders arising from encoding and imparting the discrete phase mask in equation 3.1 onto the LCD depends on the N discrete phase levels. There are some orders that have zero intensity weighting depending on the phase level. To solve the weighting coefficients of the diffraction orders, we write the following expression:

$$\exp\left(i\Phi_{Multi-level}\right) = \sum_{m=-\infty}^{\infty} c_m \exp\left(im\Phi\right), \tag{3.2}$$

where c_m is the weighting coefficient for a specific diffraction order m. For simplicity, we have to normalise the weighting coefficient c_m such that $\sum |c_m|^2 = 1$. This is solved analytically to find the desired weighting coefficients of

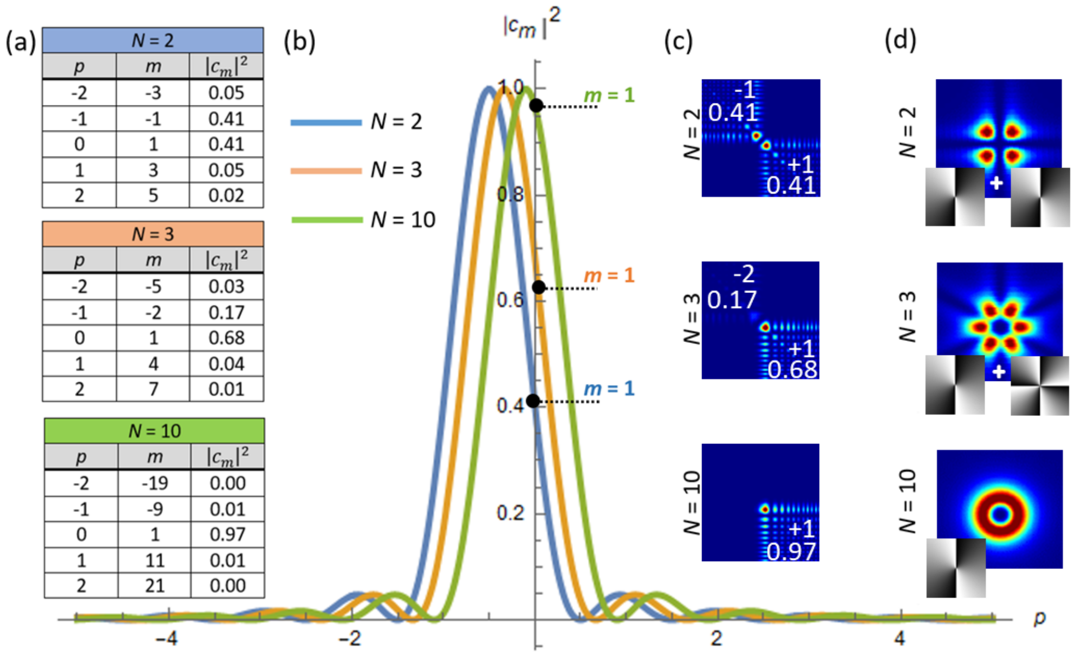

FIGURE 3.2: (a) Diffraction orders (m) with corresponding efficiencies (c_m^2) for multi-levels, $N = 2$ (top, blue), 3 (middle, orange) and 10 (bottom, green). (b) Efficiency plot versus integer p (diffraction order, $m = pN + 1$) for multi-levels, $N = 2$ (blue), 3 (orange) and 10 (green). (c), (d) Intensity profiles for cubic (Airy) and azimuthal phase variations, respectively for multi-levels, $N = 2$ (top), 3 (middle) and 10 (bottom). The values contained as inserts in the Airy intensity profiles (c) represent the diffraction order (top) and corresponding efficiency (bottom). The inserts in (d) represent the azimuthal phase profiles of the dominant diffraction orders

$$|c_m|^2 = \left[\frac{\sin\left(\frac{\pi m}{N}\right)}{\frac{\pi m}{N}}\right]^2, \tag{3.3}$$

equation 3.3 illustrates that there exists harmonic orders given by the term $m = pN + 1$, where n is any integer assigned with the intensity $|c_m|^2$. Each order is a result of a transmission function given by Φ where p decides which order may contain the power content $|c_m|^2$ and the rest will not have any output power (null intensity). Let us take a very specific example when $N = 2$, the orders that will have an output power will be $m \in \{..., -5, -3, -1, 1, 3, 5, ...\}$ with the respective phase functions of $(.., -5\Phi, -3\Phi, -1\Phi, 1\Phi, 3\Phi, 5\Phi, ...)$ and so on. Because of the linearity of equation 3.2 and the linearity of Fourier optics, the far-field pattern of the final segmented function is the combination of the far-fields of each harmonic order. To show the linearity example, we chose the three example test cases, these includes an axicon phase for 0^{th} order Bessel beams, a cubic phase for Airy beams and an azimuthal phase for vortex beams. The three modes are identified by the following equations:

$$\Phi_{Axicon} = -k_r r, \tag{3.4}$$

$$\Phi_{Cubic} = \left(\frac{x}{\omega_0}\right)^3 + \left(\frac{y}{\omega_0}\right)^3, \tag{3.5}$$

and

$$\Phi_{Azimuthal} = \pm l\Phi. \tag{3.6}$$

In the case of the axicon phase in equation 3.4 r is the radial coordinate $(r = (x, y, z))$ and k_r is the radial wave-vector $\left(k_r = (k_x, k_y, k_z)\right)$. The radial wave-vector can be determined from the following expression

$$k_r = k(ni - 1)\gamma. \tag{3.7}$$

From equation 3.7 ni is the refractive index of a material the laser beam is incident onto, γ is the opening angle of the axicon. For the cubic phase, x and y are the cartesian coordinates and ω_0 retains its definition as the beam waist. The azimuthal phase is already discussed in Chapter 2. Examples of the existing diffraction orders and their efficiencies for multi-levels of $N = 2, 3$ and 10 are shown in figure 3.2. If we consider the case of the 2^{nd} multi-level $(N = 2)$, and concentration on the $\pm 1^{st}$ orders generated, they will both have equal efficiencies of 41% of 81% in total. The rest of the 19% efficiency is distributed across all other diffraction orders generated. This is evident from the table in figure 3.2 (a) and the blue plot in (b). It is also shown when viewing the on-axis intensity profiles in the top images of figure 3.2 (c) and (d). in the cubic phase case, when $(N = 2)$, we can see two Airy intensity profiles diagonal to each other representing two diffraction orders $(m = \pm 1)$, each possessing equal efficiency of 41%. As shown in (c), the efficiency in the 1^{st} order of the Airy beam increases with increasing N-steps. The intensity profile seen in the azimuthal phase (for $l = \pm 2$ and $N = 2$) also contains superimposed $(m = \pm 1)$ orders with equal efficiency (41%), and also contains 4 intensity lobes (petal-like beams), with the number of lobes dependent on the topological charge $(N|\ell|)$ [top image of figure 3.2 (d)]. As the multi-level steps (N) increases the lobes become finer, until it approximate a vortex beam. From figure 3.2 (b), we notice that as the multi-level steps increases (N), the peak of the sinc function shifts towards the origin, as seen by the orange $(N = 3)$ and green $(N = 10)$ curves in figure 3.2 (b), the corresponding existing diffraction orders and efficiencies presented in the middle and bottom tables of (a). In viewing the Airy intensity profiles [figure 3.2 (c)], the energy in the 1^{st} diffraction order $(m = 1)$ increases from 68% for $N = 3$ to 97% for $N = 10$. The same occurs for the diffraction orders ($m = 1$ and $m = -2$ superimposed) for the azimuthal phase case (with the corresponding efficiencies of 68% and 17% respectively), producing 6 lobe structure given by:

$$lobe_{number} = |m_1|\,|l_1| + |m_{-2}|\,|l_{-2}| = |1|\,|2| + |-2|\,|2| = 2 + 4. \tag{3.8}$$

Consider the example of an axicon, since the axicon transforms the incoming light into a Bessel beam with an electric field proportional to $J_q(k_r r)$, where J_q is the q^{th} order Bessel function. The experiments we conducted in the lab revolved around the 0^{th} order Bessel function, where $q = 0$. For higher order Bessel functions $(q > 0)$, these beams have a non-diffracting null intensity core, rather than the "central maxima" Gaussian core [139]. The transformation of the segmented equivalent is a sum of the Bessel functions with altered radial wave-vectors, $\sum_m c_m J_0(mk_r r)$, and similarly for the other functions. Note that in general c_m is complex and depending on the transmission function, the terms may interfere constructively or destructively. The result on the CCD camera detector is the intensity profile of this superposition. This differs from our usual interpretation of binary optics, where the structure of the light is diffracted to different locations in space. Here the beams all overlap in the same position, but have altered internal structure as per diffraction order (m).

3.3 Experimental setup

The experimental setup used to simulate multi-level DOEs is shown in figure 3.3. Various multi-level DOEs were encoded on the LCD seen in figure 3.3. An incident Gaussian beam ($\lambda \approx 633\ nm$) was expanded through a $12\times$ telescope ($f1 = 25.4\ mm$, $f2 = 300\ mm$), before illuminating and overfilling the LCD. Three types of multi-level DOEs structure that are investigated consists of an axicon phase (Φ_{Axicon}), the cubic phase (Φ_{Cubic}) and the azimuthal phase ($\Phi_{Azimuthal}$) (examples of which are given as inserts next to the LCD in figure 3.3). For the azimuthal phase mask [case(3)], the $12\times$ telescope was removed as the LCD does not require to be overfilled with a flat wavefront. This means that lens ($L1$ and $L2$) were removed, however, this is not shown in figure 3.3. In conducting the experiment, a blazed grating was added to the phase masks to separate the diffracted orders from the 0^{th}. The generated (Φ_{Axicon}) intensity profile mode at the plane of the LCD was then relay-imaged by a 4-f imaging system consisting of lens $L3$ and $L4$ with each having a focal length of ($f3 = 200\ mm$ and $f4 = 200\ mm$). The desired 1^{st} order diffraction mode was spatially filtered by the aperture, marked A, while all other unwanted orders were neglected. The resulting intensity images were then captured using a CCD camera (Grasshopper3 GS3-U3-28S4M). For the acquisition of the Bessel modes, resulting from (Φ_{Axicon}), the CCD camera was placed at a distance $\frac{1}{2}z_{max}$ after the 4^{th} lens ($L4$) where $z_{max} = \omega_0 \frac{k}{k_r}$, where k is the wave number. The Fourier transform of the Bessel mode was then acquired by placing a Fourier transforming lens ($L5$) a distance of one focal length ($f5 = 150\ mm$) from the position of $\frac{1}{2}z_{max}$ as shown in figure 3.3. While for the cubic phase (Φ_{Cubic}) and the azimuthal phase ($\Phi_{Azimuthal}$), the CCD camera was placed at the focal plane of lens ($L5$), which was positioned one focal length ($f5 = 150\ mm$) from the image plane after lens ($L4$), so as to obtain the Fourier transform of the field produced at the plane of the LCD. For each of the three types of multi-level DOE phase masks that were investigated, the number of multi-level orders (already outlined in section 3.3) were increased from $N = 2$ to $N = 10$ in a dynamic and automated approach. In the results section, we will quantitatively investigate the intensity profiles generated by the three different phase masks for various multi-level orders (N). In the case of the field produced by the axicon phase (Bessel beams), for convenience, we will use the field propagated a distance $\frac{1}{2}z_{max}$ after the image plane of the LCD, while it's Fourier transform as already explained results in an annular ring. The Fourier transform of the LCD encoded with the cubic phase and the azimuthal phase, will result in the Airy and the vortex fields, respectively.

3.4 Experimental results and conclusion

In this section we are going to cover the experimental results for the three DOE phase structures. We are also going to analyse the lowest possible multi-level (N) steps it takes to generated an approximated continuous field of each multi-level discrete fields. The experimental and the theoretical results are shown in figures 3.4, 3.5 and 3.6. Figure 3.4 shows the Bessel beams and annular rings produced by the multi-level axicon phase (Φ_{Axicon}) in the near-field and the far-field respectively. In this experiment, two axicon cone angles were used, namely $\gamma = 0.0030$ radians (top set data in figure 3.4) and $\gamma = 0.0015$ radians (bottom set data in figure 3.4). A tighter cone angle ($\gamma = 0.0015$) results in a more 2π phase variations over a given area of the axicon phase mask (Φ_{Axicon}) which is evident in comparing the top and

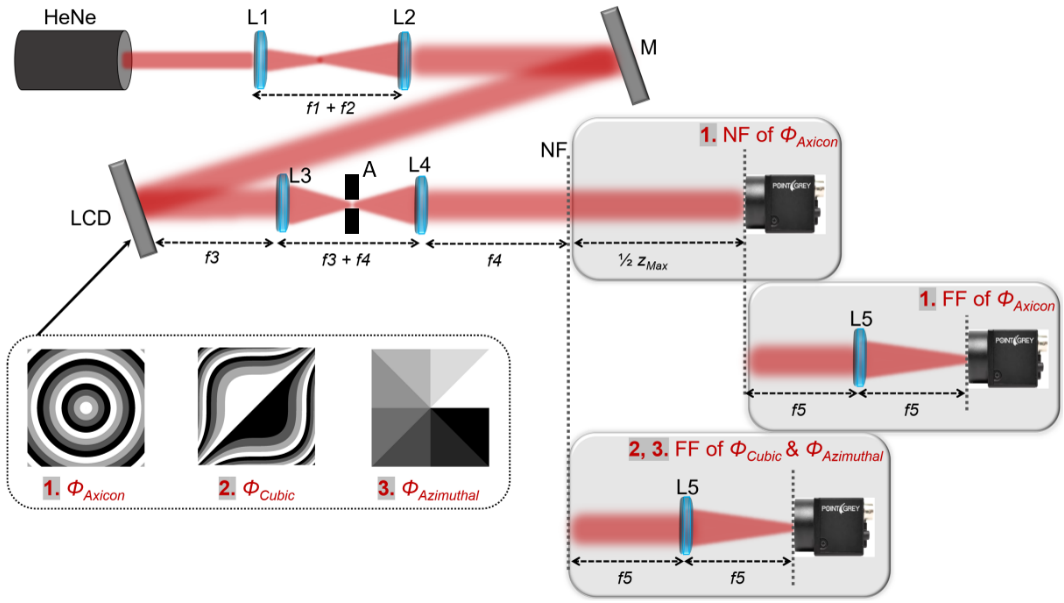

FIGURE 3.3: A schematic diagram illustrating the experimental setup we used. Various modifications of the data acquisition configuration is illustrated with the grey-shaded blocks. The Bessel beams were generated in the $\frac{1}{2}z_{max}$ region as indicated by 1 near-field (NF) of Φ_{Axicon}. The 5^{th} lens ($L5$) was used to obtain the Fourier transform of the LCD, which is the annulus labeled as 1 far-field (FF) of Φ_{Axicon}. Both the cubic and azimuthal fields were generated by placing lens ($L4$ and $L5$), ($L4 + L5$) apart from each other, and the CCD detector was placed in the focal plane of $L5$. This is demonstrated in the label 2, 3 FF of (Φ_{Cubic} and $\Phi_{Azimuthal}$). The aperture (A) was used to filter out all other undesired diffraction orders and only pass through the 1^{st} desired order.

bottom rows of the two data sets. The axicon cone angle of the generated fields affects the propagation distance that is required to generate Bessel beams in the near-field. In this case, the cone angles of the multi-level axicon phase masks are given by (z_{max} = 28.80.6 mm and z_{max} = 57.80 mm), for the cone angles $\gamma = 0.0030$ and $\gamma = 0.0015$ radians, respectively. The propagation distance needed to generate the Bessel beams also affects the total number of concentric rings in the near-field, and the size of the annular ring in the far-field as seen in figure 3.4. The number of multi-level steps used to generate the axicon phase masks (Φ_{Axicon}) increases from left to right in figure 3.4, from $N = 2$ until $N = 10$. The top panels in figure 33.4 are the axicon phase masks (Φ_{Axicon}) that evolve to approximate the 'continuous' axicon phase. The multi-level steps are easier to distinguish from the top panel data in each cone angle as shown in figure 3.4 as compared to the bottom intensity profile panels. For a higher cone angle ($\gamma = 0.0030$ radians), it can be seen with the intensity profiles that only a single 2π phase variation is present across the phase masks encoded on the LCD. Although the cone angles of an axicon multi-level phase masks might be different, a similar effect occurs for both angles in the near-field and the far-field. We observed that from the multi-level step of $N = 5$ for both cone angles in the far-field (Bessel beams) and near-field (Annulus) approximates to those generated with a continuous phase axicon cone angles.

The next multi-level DOE structure is another solution to the paraxial wave equation, which is known as the cubic phase (Φ_{Cubic}) for Airy beams. The multi-level

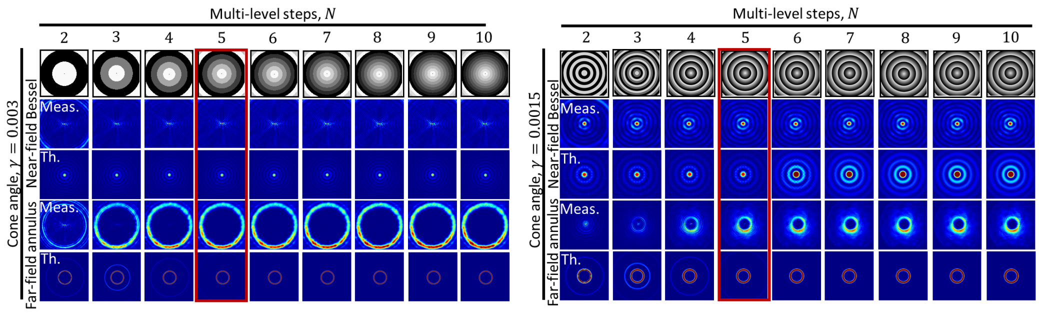

FIGURE 3.4: Multi-level of an axicon phase mask (Φ_{Axicon}) in both the near-field (Bessel beams) and the far-field (Annulus) for axicon angles ($\gamma = 0.0030$ and $\gamma = 0.0015$) radians, respectively. As the phase steps (N) increases from left to right, the multi-level axicon phase mask (Φ_{Axicon}) approximates the continuous axicon phase profiles. Even though the two axicon angles that are used in the experiment results in a different 2π phase variation over a given area of the axicon phase mask, they both approximate the continuous axicon phase profiles from $N = 5$ steps. The gray shaded data in the 1^{st} row shows the axicon phase masks at different phase level steps (N). The 2^{nd} and 4^{th} rows for each axicon angle represents the measured intensity profiles of the Bessel beams (near-field) and the annulus (far-field) respectively. The 3^{rd} and 5^{th} rows (for both axicon angles) represents their theoretical counterparts. The red solid border lines represents the phase level N where both the Bessel beams and the annulus have approximated the 'continuous' axicon phase profiles. The blazed grating accompanying the phase masks when encoded on the LCD, has been removed to aid visualisation of the multi-level DOE structure.

cubic phase mask (Φ_{Cubic}) airy beam was generated in the far-field as illustrated in figure 3.5. The number of the multi-level phase steps increases from left to right in figure 3.5 with the same N steps in figure 3.4 ($N = 2$ to $N = 10$). Airy beams can be experimentally generated using the following equation:

$$\Phi_{Cubic} = \exp\left[-\beta\left(\frac{x^2+y^2}{\omega_0^2}\right)\right]\exp\left[i\left(\frac{x^3+y^3}{\omega_0^3}\right)\right]. \tag{3.9}$$

Equation 3.9 is a cubic phase equation to generate Airy beams, which involves the addition of a cubic phase (Φ_{Cubic}) and the input Gaussian beam. Note that in equation 3.8, there is a parameter β which controls the power distribution of the Airy beam.

We generated the Airy beams in the absence of the β parameter, which was done by Fourier transforming the plane of the LCD with a lens (far-field) plane. The energy of the Airy beam in this case depended on the encoded beam size (ω_0). The multi-level phase mask hologram encoded on the LCD has the following expression,

$$\Psi_{Cubic} = \text{mod}\left(\frac{x^3+y^3}{\omega_0^3}, 2\pi\right) - \text{mod}\left(\frac{x^3+y^3}{\omega_0^3}, \frac{2\pi}{N}\right). \tag{3.10}$$

Since the 2π phase variation is very fine in the outer regions of the cubic phase function, it is very difficult to visually differentiate the multi-level steps (in the cubic phase profile, top row of figure 3.5) from $N = 5$ onwards. Similarly, as in the case of the multi-level axicon phase mask, the Airy experimental intensity profiles (2^{nd} row) agrees with the theoretical counterparts in the last row in figure 3.5.

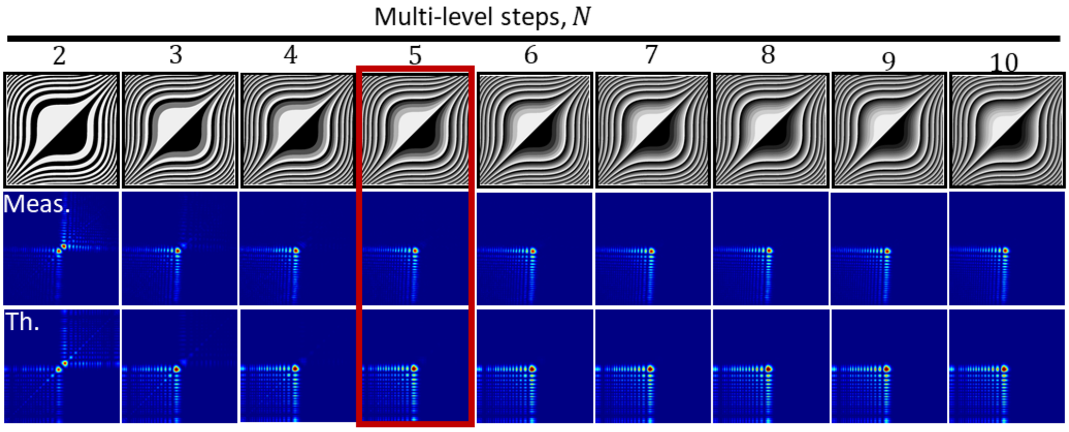

FIGURE 3.5: Phase masks for various multi-level steps (increasing from left to right) are contained in the top row with the resulting far-field intensity profiles contained in rows $(2-3)$. The red solid border line illustrates where multi-level cubic phase mask (Φ_{Cubic}) approximates the continuous cubic phase. The blazed grating accompanying the phase masks when encoded on the LCD, has been removed to aid visualisation of the multi-level diffractive optical element structure.

The azimuthal multi-level phase masks ($\Phi_{Azimuthal}$) is generated in the far-field. The multi-level steps N also ranged from $N = 2$ to $N = 10$ as illustrated in figure 3.6, which increases from left to right. Here, the azimuthally varying phase $\exp(i\ell\Phi)$ of the varying topological charge (ℓ) was increased from top to bottom ($\ell = 1$ to $\ell = 4$) as shown in subsequent rows of figure 3.6. As the topological charge increases the multi-level step (N) required to approximate the continuous azimuthal phase decreases. This means that it will take less steps to complete the approximation with higher ℓ than with a much lower one.

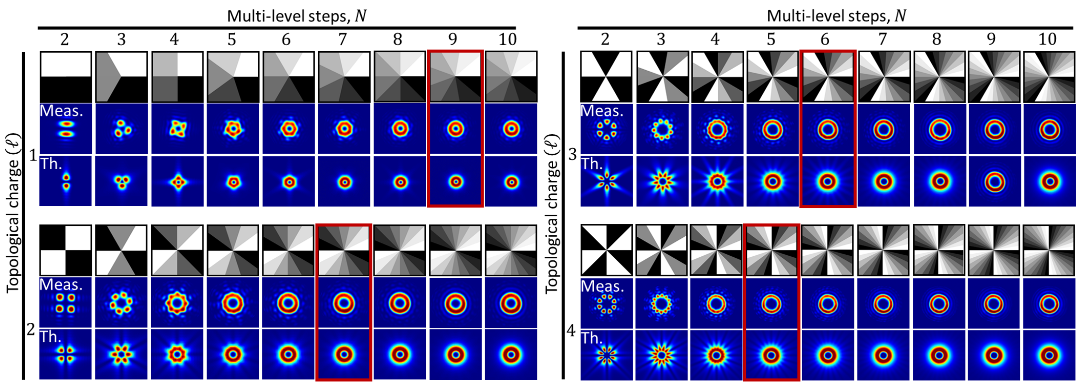

FIGURE 3.6: Topological charges varying from $\ell = 1$, 2, 3 and 4 are contained. Phase masks for various multi-level steps (increasing from left to right) are contained in the top rows, while the resulting far-field intensity profiles are contained in the accompanying bottom rows. The red solid border lines in each topological charge ℓ illustrates the multi-level step required to approximate the continuous phase modes. The blazed grating accompanying the phase masks when encoded on the LCD, has been removed to aid visualisation of the multi-level DOE structure.

Summary, we have generated various multi-level spatial structures on a LCD, through the simulation of the multi-level DOE. The generated DOE structures consist of an axicon, cubic and azimuthal phase profiles, and we investigated their resulting intensity profiles. We also showed that we only require a few multi-level steps to approximate the same spatial modes that are generated via ’continuous’ phase profiles.

Chapter 4

Segmented phase-shaping

4.1 Introduction to deformable mirrors

Early observations in space using old telescopes were greatly limited by the effects of turbulent media as light propagated into the Earth's atmosphere. The limitations were due to regular variations in the refractive index as a result of constant changes in the temperature. This change in temperature caused the effects of atmospheric turbulence. The effects of turbulence causes scintillation effects [140] or blurry output images. A deformable mirror device is used to rectify this display error and produce a much clearer or visible image output[115], [141], [142].

The first concept of a deformable mirror was used in projection of television in 1943 and it was produced by a Professor Fritz Fischer [143], [144]. This device is known as an "Eidephor system", the Eidephor was made of a thin glass surface coated with a protective oil film. The oil coating is known as the Eidephor, which deforms when the electrostatic forces are applied onto it and assumes a desired deformation for better output video signals.

It was the Eidephor invention that motivated Horace Babcock in 1953 to propose the first deformable mirror [121], which involved the reshapable reflective surface located in a plane conjugate to a telescope mirror which is designed to rectify the blurriness (scintillation effect) output images caused by the atmospheric turbulence. The first deformable mirror was fabricated from a glass substrate surface coated with a reflective protective metal substrate, attached to piezoelectric actuators [13]. Even in the midst of high expense and rather difficult to fabricate, these deformable mirror devices cancelled the scintillation effects and transformed the astronomical telescopes at that time.

Micro scaled deformable mirrors also revolutionized through the MEMS based technology. MEMS based deformable mirrors are made of very small micromirror pixels, wavefront sensors and silicon based plates or wafers that acts as actuators. In 1994 Boston university received funding from the defense advanced research project agency to fabricate micro scaled deformable mirrors which are much cheaper with more actuator strokes, and relatively smaller than their bulky conventional counterpart. In the year 1999, Boston university ventured in a company known as Boston micromachines corporation and made the deformable mirrors commercially available [13].

There are different types of deformable mirrors used for phase control, but the most commonly used are the bimorph and piston-only deformable mirrors. The bimorph base deformable mirrors are made of two poled piezoelectric ceramic wafers coated with a flexible glass sheet that is deformable to achieve phase control. Piston deformable mirrors are made of segmented rigid array of mirrors which can be independently controlled to achieve a certain level of actuator stroke to obtain phase control. The segmented mirrors comes in various mirror configuration such as (cartesian, polar, hexagonal, etc.)[145]. Since the segmented mirrors in the piston-based model are rigid, they do not undergo a deformation, instead the array follows a controlled deformation pattern through different actuation strokes controlled by an applied voltage to each mirror electrode [17].

The simplest deformable mirror device implemented for phase control and phase modulation are the segmented deformable mirror devices due to their simple operation to control each actuator independently [118] which can approximate many phase structures and they are less costly and easy to operate unlike their continuous facesheets counterpart which are quite expensive and difficult to operate since the actuators are mechanically coupled and dependent on each other for phase control[146]. Even though segmented deformable mirrors cause light to diffract due to spacing between the segments [147], they are ideal for phase singularity beam shaping since the segments can be individually controlled to assume a spiral configuration. They are made up of various geometric apertures (Cartesian, polar, and even hexagonal) consisting of N segmented mirror pixels attached to an actuator system [145].

There has been reported use of deformable mirrors for beam shaping. Robert et al reported the generation of optical vortices by using an Iris AO S37-X deformable mirror consisting of 37 hexagonal actuators [148] with a HeNe laser beam ($\lambda \approx 633$ nm). They formed a discontinuous reflective surface by digitally entering the mirror position of each actuator which allows the device controller to assume a spiral configuration in a piston-tip-tilt fashion. A Michelson interferometer was used to produce an interference pattern between the reference plane wave and the plane wave carrying an OAM beam to verify the topological charge in the pupil plane [149]

The generation of BG beams was reported by Xiaoming Yu et al, they used a segmented deformable mirror with 37 hexagonal segments in a honeycomb configuration to generate a 0^{th} and higher order Bessel beams by following two experimental procedures. They first used the deformable mirror as a reflective axicon to generate the 0^{th} order Bessel beam, and then they optimized the shape of the deformable mirror to generate a 2π spiral phase shift to generate higher order Bessel beams [150]. Even though deformable mirrors have been demonstrated as beam shapers, the spatial mode profiles generated with these devices often have low beam fidelity or low correlation with their desired theoretical counterparts.

In this work we use the LCoS-SLM as a testbed to mimic and subsequently investigate the parameters that affect beam shaping with deformable mirrors, such as the segment geometry and the number of segments.

4.2 Mimicking the deformable mirror with LCoS-SLM

Figure 4.1 and figure 4.2 shows how the two deformable mirror segmented geometries were formed on the LCD screen. Figure 4.1 represents the OAM phase (a vortex beam with topological charge = 3) imparted on a segmented polar geometry, this geometry is made up of two Degrees of Freedom (DoFs), the azimuthal and the radial

DoFs respectively. The azimuthal DoFs is used to select the number of core segments, and the radial DoFs is used to determine the number of concentric segments desired to shape light. By adding the two DoFs together we obtain the polar segmented geometry on the left with an imparted vortex phase. Figure 4.2 illustrates the cartesian geometry with the same phase profile encoded. This is also made up of two DoFs, the n_x, which dictates how many segments are required along the x-plane, and the n_y which dictates the number of segments required along the y-plane. By multiplying the two DoFs will result in the segmented cartesian geometry on the left with an imparted vortex phase profile.

The experimental setup seen in figure 4.3 illustrates how we generated segmented spatial modes using the LCD. The experimental data was taken in the far-field (Fourier plane) for three different phase profiles, the OAM phase (vortex beam, with OAM = 3), the cartesian flattop beam and the annular ring. The phase profile is divided into N-segmented arbitrary configuration, where each segment depicts a linear actuator within a deformable mirror array. This is illustrated by the phase profile with square mirror arrays in figure 4.3 under "segmentation", where N is the total number of the mirror arrays. The segmented hologram encoded onto the LCD in figure 4.3 is the vortex beam imparted on a 10×10 $\left(N = 10^{10}\right)$ cartesian modulator. The experiment was conducted with the same SLM, CCD camera and laser beam already defined in Chapter 3. Each actuator has to follow or abide to the following equation, to successfully alter the phase of an incident light:

$$\Phi = \frac{2\pi D}{p\lambda}, \tag{4.1}$$

where $\frac{D}{p}$ is the discrete steps, D is the actuator stroke, λ retains its previous definition and p is the segment precision. Most commercially available deformable mirrors display a 5 μm actuator stroke with a 1 nm stroke control.

We saw that the number of segments affected the transverse intensity profile of a beam generated. At low number of segments like the one seen in figure 4.3 next to the CCD camera, the intensity profile which is supposed to be a vortex beam is indistinguishable. It is also seen that the energy of the beam is not concentrated into the region of interest, which may result in efficiency losses as well. We use the same FoM used in equation 2.27 to quantize the ability of the modulator to generate high purity beam(s). In the next section we will analyse the effects of the segment number and the segment geometry on the FoM of the generated transverse beam profiles for a vortex beam, cartesian flattop beam and the free OAM annular beam.

4.3 Experimental results

Figure 4.4 represents the cartesian flattop transverse profile generated on a cartesian geometry modulator. The plot below represents the dependence of the FoM on the number of segments, which illustrates that the number of segments and FoM in this case are directly proportional. At low number of the segments, the ability of the modulator to generate a high fidelity transverse intensity profile is limited. This can be seen with the first transverse intensity profile on the left in figure 4.4, whereby a large portion of the beam's energy moves away from the region of interest which causes some maxima lobe regions on both sides of the $1D$ cross-intensity plot. The corresponding phase profile shows that the segments are not aligned with the phase discontinuities as compared to the last phase profile on the far right. However, as the

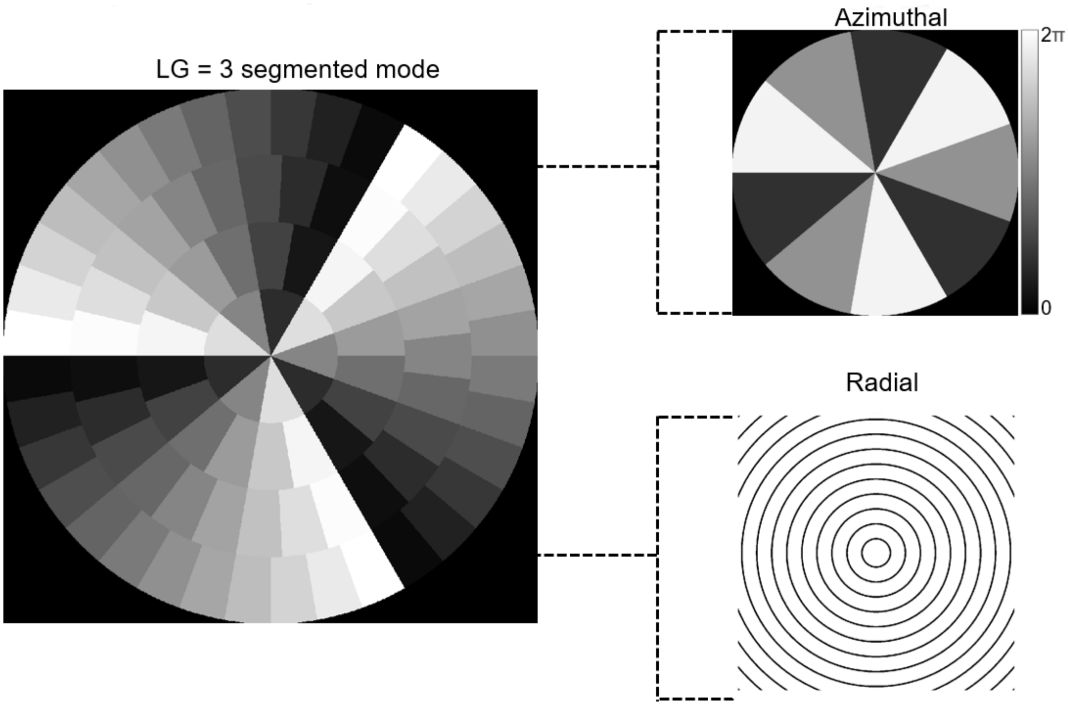

FIGURE 4.1: A demonstration of how the polar segmented deformable mirror geometry is formed. It takes two DoFs to form the radial segmented configuration seen on the left with an imparted spiral phase, these are the azimuthal and the radial DoFs. The azimuthal DoFs defines the core segments, while the radial DoFs defines the angular segments. The segments increases linearly in each concentric ring. We chose 4 angular segments and 9 core segments ($N = 90$) for a clear visualisation of both the azimuthal and the radial DoFs as they increase.

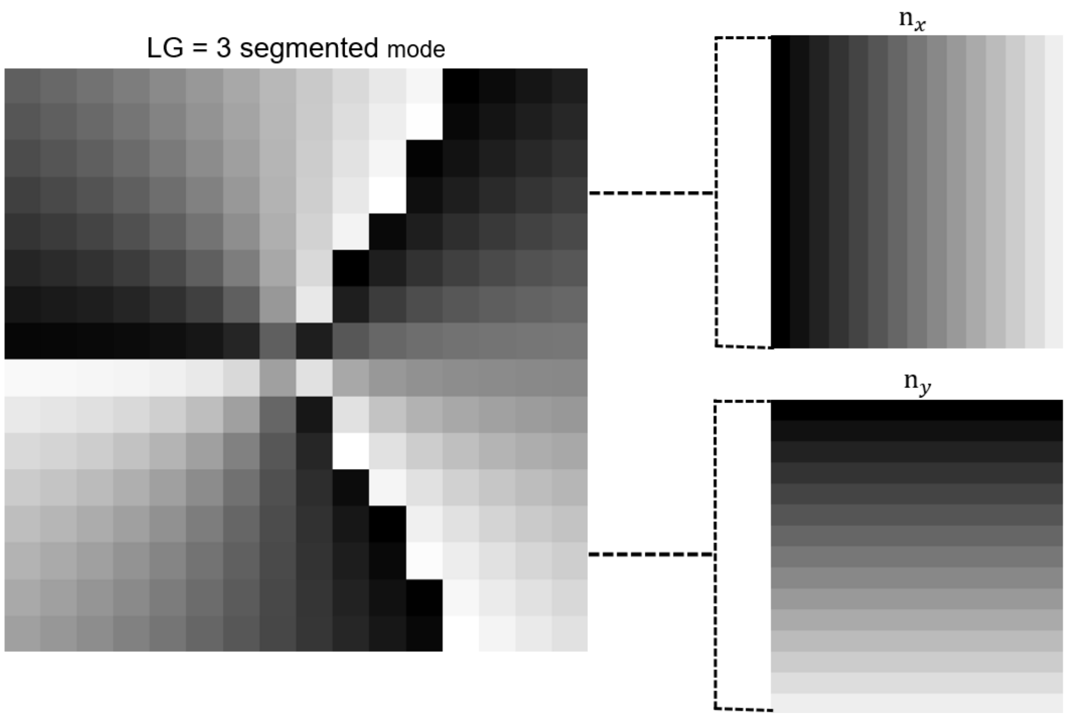

FIGURE 4.2: A cartesian segmented geometry is also made up of 2 DoFs, the n_x which controls the number of segments required along the x-plane and the n_y which controls the number of segments along the y-plane. By multiplying these DoFs together, we obtain the segmented spiral phase on the left. Here, we chose a 16×16 ($N = 256$) segmented array, which forms a square grid. The lower number of segments makes it better to clearly see the segments.

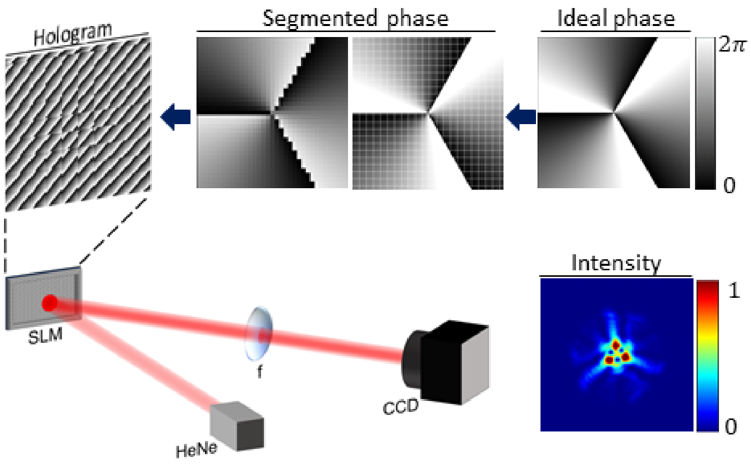

FIGURE 4.3: An illustration of how the cartesian geometry modulator generates a vortex beam with topological = 3. The ideal phase profile is divided into a given number of segments with each segment taking on the nearest phase permitted by the actuator stroke precision. The computer generated hologram is encoded onto a 10×10 segmented array, and we can clearly see that with the given segments, the ability of the modulator to approximate a vortex beam generated with a continuous phase is limited. The first order is focused onto the CCD camera sensor with a lens with a focal length f. The modulator in this case is the SLM used to simulate how an ideal $\left(N = 10^{10}\right)$ segmented deformable mirror would be used to generate a vortex beam (OAM = 3)

number of segments increases the energy of the beam is concentrated into the region of interest which results in a high beam fidelity represented as FoM. The main aim of figure 4.4 is to investigate the effects of the mirror segments on the ability of the modulator to produce good fidelity modes.

Now that we explored that we could produce a high fidelity beam shaping with a segmented modulator, provided there are enough segments to capture the transverse phase profile of a beam. We still have to explore the effects of geometry on structured light, this aims to find out which deformable mirror geometry would be more efficient (less segments and less bulky) to buy or manufacture for a specific beam shaping application. In figure 4.5 we evaluate which geometry produces three phase structures (cartesian flattop beam, free OAM annular beam and the vortex beam) with less segments. Here, we kept the FoM fixed (0.9), this means that for each segment geometry for each phase profile, we altered the number of segments until we obtain FoM threshold of 0.9. Figure 4.5 shows that the segmented geometry that matches the geometry of the phase profile is superior, provided there are enough segments to capture the transverse phase profile of the generated phase structure. This is seen in the case of the cartesian flattop beam where the cartesian geometry is seen to be superior. In the case of a free OAM annular ring which is radially symmetric, the polar geometry is superior over the cartesian geometry. For a non-symmetric vortex beam with OAM $= 3$, the geometry that generates a high fidelity vortex beam with less segments to capture the transverse phase profile is superior, in this case, the polar segmented geometry. The choice of OAM $= 3$ is arbitrary. The $1D$ cross-section plots seen in each transverse intensity profiles, shows the agreement between theory (black plot) and experimental data (red plot). The white text seen in each intensity profile in figure 4.5 illustrates the number of segments required to produce beam profiles with $FoM = 0.9$.

In figure 4.6, we intend to investigate the ability of the segmented modulator to shape light as the transverse phase profile rotates. We can see that that as the phase profile rotates, the segments misalign with the phase discontinuity of the spiral phase (OAM = 3). The misalignment causes artifacts on the segmented phase (when $\theta = 12°$). The spiral phase is rotated over the following angles, 0°, 12° and 40° with the same number of segments used to generate a vortex beam on a polar geometry in figure 4.5. Now that we see there may be a misalignment between the segments and the phase discontinuity for a spiral phase as it rotates through θ, this means at some angles, the intensity profile of the vortex beam will be indistinguishable as a result.

Figure 4.7 shows the resulting intensity profile of the vortex beam and its phase counterpart as it rotates along θ. The FoM varies over three angles (12°, 20° and 40°), only at 12° and 20° the intensity profile is indistinguishable and looks abberated. This means that the ability of the modulator to generate a vortex beam is limited at specific angles. This changes when the segments aligns with the phase discontinuities at ($\theta = 40°$), which is followed with an increase in FoM.

We explored the effects of the segmented deformable mirror geometry and the number of segments on beam shaping. We have successfully demonstrated a simulation of the segmented deformable mirror on a LCoS-SLM. The measured results agreed with the theoretical results. We have also explored the relationship between the segment configuration and the desired phase structure. For a radially symmetric phase structures, we may require less segments to obtain a high fidelity mode, as compared to using a cartesian segments and vice versa. In a case whereby a phase structure is non-symmetric, the segment geometry that aligns with the phase discontinuities with less number of segments is preferred. This work will act as a map to either buy or manufacture a deformable mirror for a desired beam shaping using high-power laser beam(s).

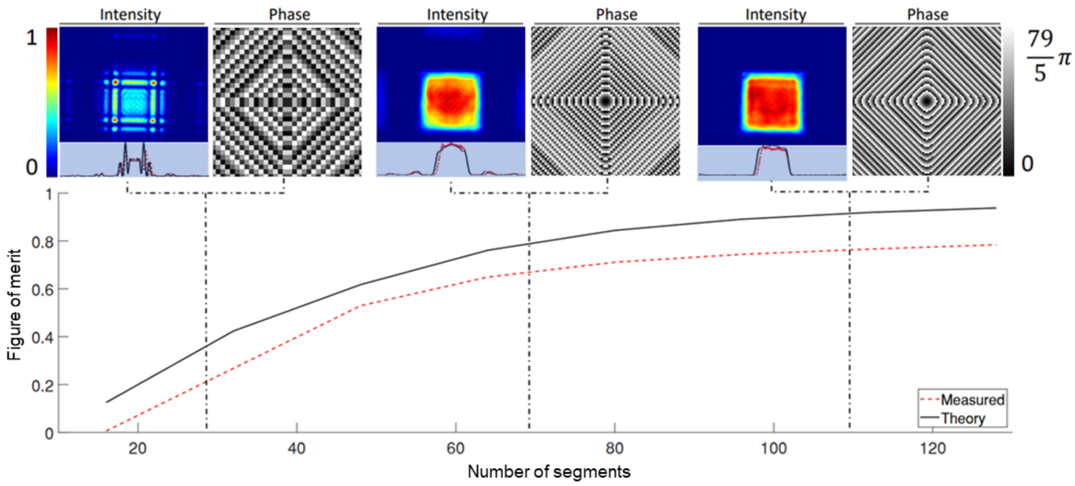

FIGURE 4.4: The plot seen below the transverse intensity profile and the phase profile panels illustrates the dependence of the FoM on the number of segments. Here, we see how the cartesian flattop beam improves as the number of segments increases for three segment regions which are, 32, 64 and 112. At low number of segments, we see that the energy of the flattop beam moves away from the region of interest, which causes a huge deviation from the ideal, desired flattop beam profile. The intensity profile in the first intensity panel has lobes on each sides, which represents the loss of energy from the region of interest. When the number of segments increases, this energy is concentrated into the region of interest, and lobes seen in the first intensity panel decreases, resulting in a much flatter profile. The offset between the theoretical curve (black curve) and the experimental curve (red dashed curve) is due to the dynamic range of the camera.

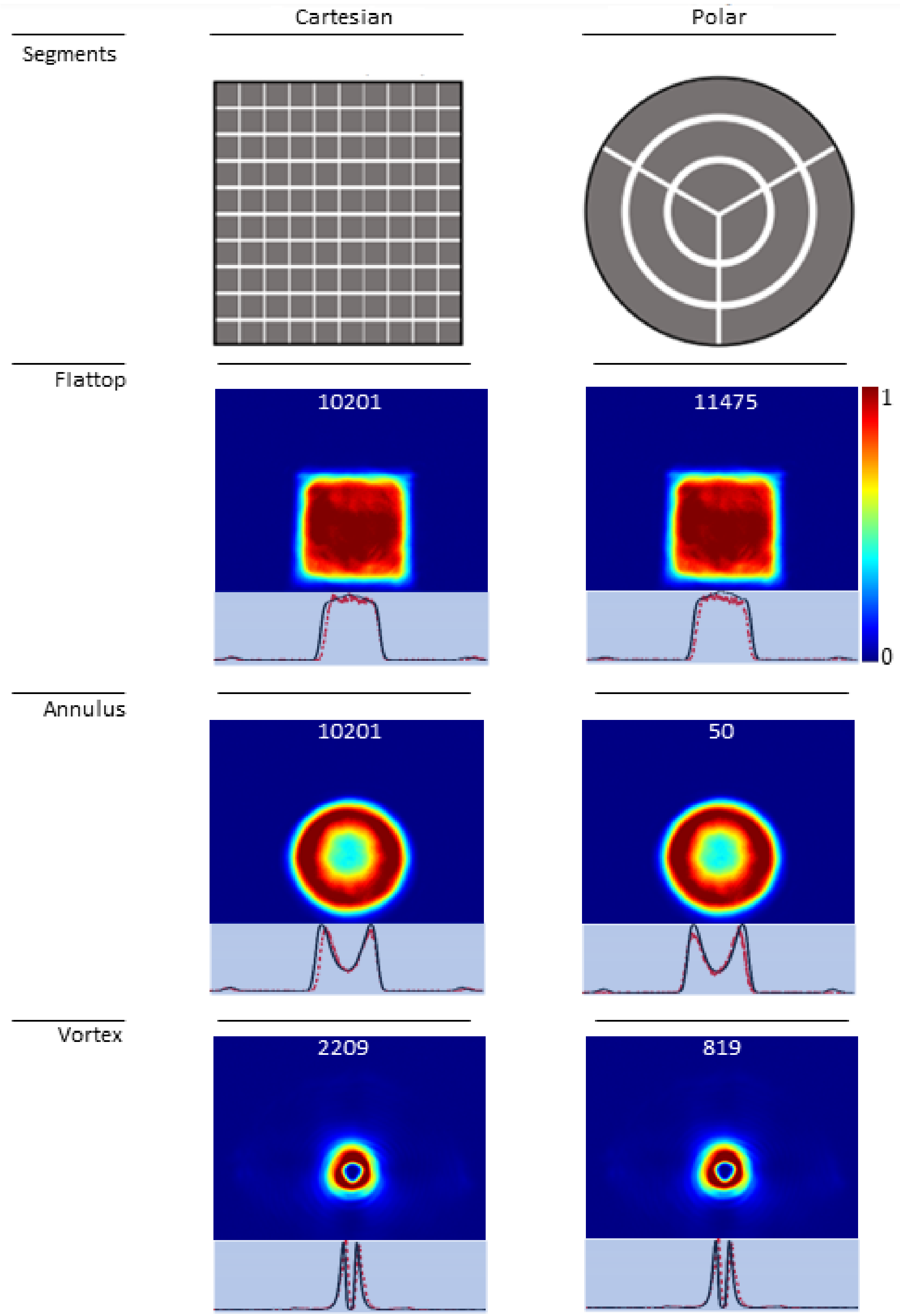

FIGURE 4.5: We compare two segmented configurations (cartesian and polar geometries) to analyse which geometry produces a high fidelity with less segments. Deformable mirrors with many segments can be costly and bulky, this serves as a map to know which geometry and the number of segments required to produce a beam with high fidelity. The number of segments are shown inside each intensity panel. A cartesian geometry would be preferable to generate a cartesian flattop beam, on the contrary, for a radially symmetric annulus, a polar geometry would be a best choice. In the case of a non-symmetric beam, a vortex beam with OAM $= 3$, a polar configuration is superior.

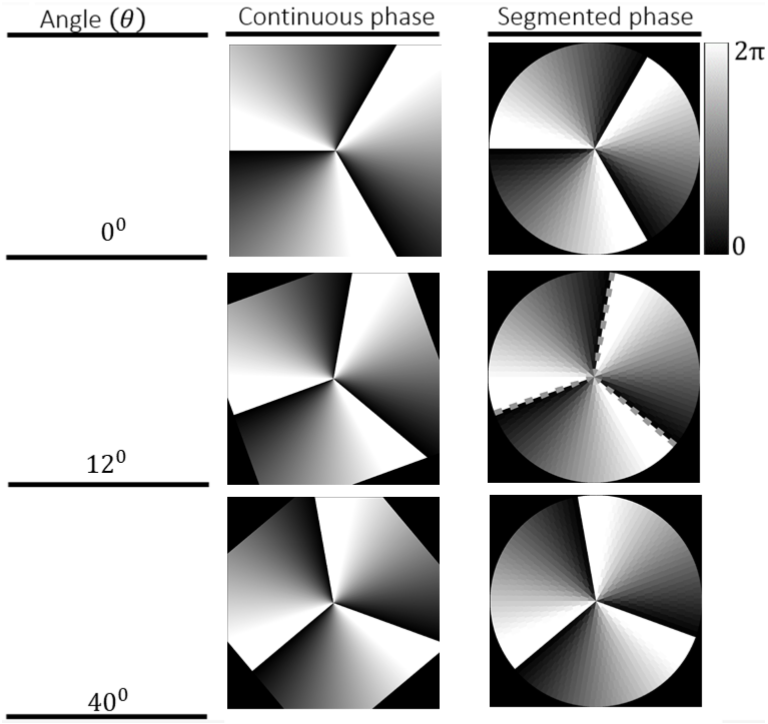

FIGURE 4.6: An illustration of how rotating the phase profile of a non-symmetric spiral profile of OAM = 3 affects the degree of aliasing. The phase profile is rotated along θ at angles 0°, 20° and 40°. The artifacts seen when the phase profile makes a 20° rotation occurs when there is a misalignment between the segments and the phase discontinuity. This will result in an abberated intensity profile

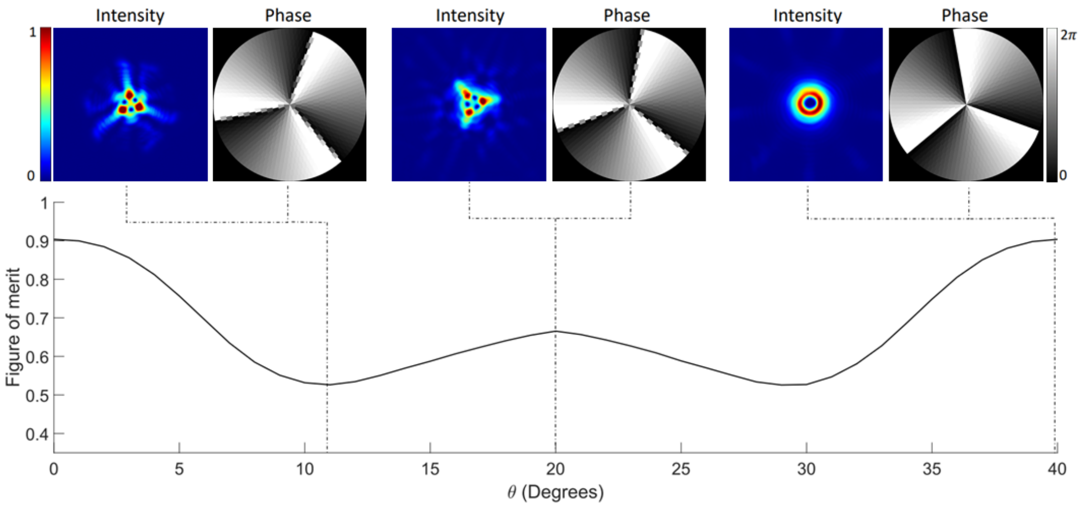

FIGURE 4.7: This demonstrates the dependence of *FoM* on the rotation of the transverse phase profile. The number of segments are kept the same for a spiral phase (OAM = 3) for the same polar geometry depicted in figure 4.5. The transverse phase profile is rotated over three angles, 12°, 20° and 40°, but only at angles 12° and 20°, we some artifacts on the phase profile, as a result of the misalignment between the segments and the phase discontinuity. This causes a low *FoM* and as a result the vortex intensity profile becomes indistinguishable. The grating function was removed to aid with visualisation.

Chapter 5

Conclusion

This work was based on using an LCoS-SLM as a testbed to experimentally simulate DoEs and deformable mirrors for beam shaping. We investigated the effects of the number of phase masks in the multi-level discrete fashion to demonstrate that we only require low phase masks to generate three mode structures (vortex beams, Airy beams, Bessel beams and annular rings). We also investigated that a mirror geometry that matches the geometry of the phase structure generated requires less mirror segments to align with the phase discontinuities to produce a high fidelity beam(s). Often time, more than necessary segments are used which can be quite expensive, bulky and time consuming to fabricate. The use of the LCoS-SLM helped to investigate the minimal amount of segments or phase masks required to shape phase structures of interest with either the deformable mirrors or DOEs.

Chapter 1 outlined a brief introduction outlining various SLM devices for beam shaping. It followed with the Maxwell's equations and how they play a fundamental role to describe electromagnetic fields required to produce various beam structures.

In Chapter 2, we discussed how to generate various CGHs that were encoded onto the LCoS-SLM. We also discussed the effects of a diffraction grating on the generated beam profiles. A Diffraction grating was seen to separate the desired modulated 1^{st} order mode away from the unmodulated 0^{th} mode to avoid interference from the 0^{th} order. We discussed how the LCoS-SLM operates and how the device is calibrated for a specific laser beam wavelength used to achieve a desired 2π phase modulation. In this work the modulator was calibrated for a ($\lambda \approx 633$ nm) laser beam wavelength. There were also demonstration of some CGHs imparted onto the LCD of the modulator, with the use of a lens, the resulting hologram produced a $2D$ intensity profile in the focal plane of the lens. With the help of diffraction grating, we were able to isolate the 1^{st} to analyse its purity. We used different FoM to quantify the beam measured in the observation plane. FoM included measuring first the beam purity, which involves how well the measured data correlates with the desired theoretical measurement. This was done by overlapping the intensity cross-sections of both the experimental and theoretical beams together, a good beam purity must produce a high correlation number. Another FoM measured was both the beam correlation and the efficiency of both the measured and the theoretical beams in the region of interest. The chapter concluded with an introduction of the deformable mirror device and its significant role to compensate for atmospheric turbulence that affects an incident field propagating in space.

In chapter 3 we demonstrated to use of the LCoS-SLM to mimic the DOEs in a multi-level discretised phase levels to investigate the number of phase masks required to approximate various phase structures generate with a continuous phase. The multi-level DOE structures were successfully achieved for three phase structures in chapter 3. The azimuthal phase (in the far-field as the vortex beam), cubic phase (in the far-field as the Airy beam) and the axicon phase (in the far-field as the annular ring and the near-field as the Bessel beam). It was seen that all three phase structures required not more than 10 multi-level steps to produce modes that are close to the ones generated with a continuous phase.

Using the SLM is convenient since we can achieve tens of thousands of phase mask steps or segments to analyze how many DoFs are required to achieve a high-fidelity phase of interest. DoFs in this case are the number of segments for deformable mirrors and number of phase masks for DOEs.

In chapter 4, we used the LCoS-SLM as well to mimic the design and operation of the deformable mirror. We addressed each pixel to assume a particular segmented geometry with certain number of segments to modulate light. Figure 4.4 illustrated the dependence between the number of segments and the FoM in equation 2.27 which are directly proportional. As we increased the number of pixel segments the ability of the modulator generated high FoM spatial beams in the observation plane. Figure 4.5 showed the relationship between the segment geometry and the transverse phase structures. The modulator generated three phase structures (the cartesian flat-top beam, vortex beam and the free OAM annular ring) in the far-field, we saw that the segment geometry that matched with the generated phase symmetry was superior provided there are enough segments to align with the phase discontinuities. For a non-symmetric structure (a spiral phase), we saw that the segmented geometry that produced a high FoM with less number of segments was superior, polar segmented geometries produced high FoM with less segments. Figure 4.7 demonstrated the effects of rotating a non-symmetric mode through θ on FoM. At some angles there were artifacts resulting from the misalignment between the phase discontinuities and the segments which introduced abberations and reduced the beam quality or FoM.

Bibliography

[1] F. M. Dickey, S. C. Holswade, and D. L. Shealy, *Laser beam shaping applications: Optical engineering*, 2006.

[2] C. Slinger, C. Cameron, and M. Stanley, "Computer-generated holography as a generic display technology," *Computer*, vol. 38, no. 8, pp. 46–53, 2005.

[3] Z. Kuang, W. Perrie, J. Leach, *et al.*, "High throughput diffractive multi-beam femtosecond laser processing using a spatial light modulator," *Applied Surface Science*, vol. 255, no. 5, pp. 2284–2289, 2008.

[4] B. R. Boruah, "Dynamic manipulation of a laser beam using a liquid crystal spatial light modulator," *American Journal of Physics*, vol. 77, no. 4, pp. 331–336, 2009.

[5] J. A. Neff, R. A. Athale, and S. H. Lee, "Two-dimensional spatial light modulators: A tutorial," *Proceedings of the IEEE*, vol. 78, no. 5, pp. 826–855, 1990.

[6] D. Casasent, "Spatial light modulators," *Proceedings of the IEEE*, vol. 65, no. 1, pp. 143–157, 1977.

[7] G. Lazarev, A. Hermerschmidt, S. Krüger, and S. Osten, "Lcos spatial light modulators: Trends and applications," *Optical Imaging and Metrology: Advanced Technologies*, vol. 1, 2012.

[8] A. D. Fisher, "Spatial light modulators: Functional capabilities, applications, and," *international journal of optoelectronics*, vol. 5, no. 2, pp. 125–167, 1990.

[9] N. Savage, "Digital spatial light modulators," *Nature Photonics*, vol. 3, no. 3, pp. 170–172, 2009.

[10] M. Kujawińska, R. Porras-Aguilar, and W. Zaperty, "Lcos spatial light modulators as active phase elements of full-field measurement systems and sensors," *Metrology and Measurement Systems*, pp. 445–458, 2012.

[11] G. Vdovin and P. Sarro, "Flexible mirror micromachined in silicon," *Applied optics*, vol. 34, no. 16, pp. 2968–2972, 1995.

[12] T. G. Bifano, J. Perreault, R. K. Mali, and M. N. Horenstein, "Microelectromechanical deformable mirrors," *IEEE Journal of selected topics in quantum electronics*, vol. 5, no. 1, pp. 83–89, 1999.

[13] T. Bifano, "Mems deformable mirrors," *Nature photonics*, vol. 5, no. 1, pp. 21–23, 2011.

[14] R. E. Morgan, E. S. Douglas, G. W. Allan, *et al.*, "Mems deformable mirrors for space-based high-contrast imaging," *Micromachines*, vol. 10, no. 6, p. 366, 2019.

[15] R. L. Knipe, "Challenges of a digital micromirror device: Modeling and design," in *Micro-optical Technologies for Measurement, Sensors, and Microsystems*, SPIE, vol. 2783, 1996, pp. 135–145.

[16] L. J. Hornbeck, "Digital light processing for high-brightness high-resolution applications," in *Projection Displays III*, SPIE, vol. 3013, 1997, pp. 27–40.

[17] M. C. Roggemann, V. M. Bright, B. M. Welsh, *et al.*, "Use of micro-electro-mechanical deformable mirrors to control aberrations in optical systems: Theoretical and experimental results," *Optical Engineering*, vol. 36, no. 5, pp. 1326–1338, 1997.

[18] M. Douglass, "Dmd reliability: A mems success story," in *Reliability, Testing, and Characterization of Mems/Moems II*, SPIE, vol. 4980, 2003, pp. 1–11.

[19] W. P. Bleha Jr and L. A. Lei, "Advances in liquid crystal on silicon (lcos) spatial light modulator technology," *Display Technologies and Applications for Defense, Security, and Avionics VII*, vol. 8736, pp. 47–54, 2013.

[20] A. Forbes, "Structured light: Tailored for purpose," *Optics and Photonics News*, vol. 31, no. 6, pp. 24–31, 2020.

[21] L. Gong, Y. Ren, W. Liu, *et al.*, "Generation of cylindrically polarized vector vortex beams with digital micromirror device," *Journal of Applied Physics*, vol. 116, no. 18, p. 183 105, 2014.

[22] Y. Tang, W. Perrie, J. Schille, *et al.*, "High-quality vector vortex arrays by holographic and geometric phase control," *Journal of Physics D: Applied Physics*, vol. 53, no. 46, p. 465 101, 2020.

[23] J. F. Algorri, V. Urruchi, B. Garcia-Cámara, and J. M. Sánchez-Pena, "Generation of optical vortices by an ideal liquid crystal spiral phase plate," *IEEE electron device letters*, vol. 35, no. 8, pp. 856–858, 2014.

[24] A. Trichili, T. Mhlanga, Y. Ismail, *et al.*, "Detection of bessel beams with digital axicons," *Optics express*, vol. 22, no. 14, pp. 17 553–17 560, 2014.

[25] R. Rop, A. Dudley, C. López-Mariscal, and A. Forbes, "Measuring the rotation rates of superpositions of higher-order bessel beams," *Journal of Modern Optics*, vol. 59, no. 3, pp. 259–267, 2012.

[26] L. Gong, Y.-X. Ren, G.-S. Xue, *et al.*, "Generation of nondiffracting bessel beam using digital micromirror device," *Applied Optics*, vol. 52, no. 19, pp. 4566–4575, 2013.

[27] N. Bhebhe, C. Rosales-Guzman, and A. Forbes, "Classical and quantum analysis of propagation invariant vector flat-top beams," *Applied optics*, vol. 57, no. 19, pp. 5451–5458, 2018.

[28] R. A. Suarez, T. A. Vieira, I. S. Yepes, and M. R. Gesualdi, "Photorefractive and computational holography in the experimental generation of airy beams," *Optics Communications*, vol. 366, pp. 291–300, 2016.

[29] L. Hu, L. Xuan, Y. Liu, Z. Cao, D. Li, and Q. Mu, "Phase-only liquid-crystal spatial light modulator for wave-front correction with high precision," *Optics express*, vol. 12, no. 26, pp. 6403–6409, 2004.

[30] H. Ma, Z. Liu, H. Wu, X. Xu, and J. Chen, "Adaptive correction of vortex laser beam in a closed-loop system with phase only liquid crystal spatial light modulator," *Optics Communications*, vol. 285, no. 6, pp. 859–863, 2012.

[31] V. Nascov, M. Kusko, D. Apostol, V. Damian, and R. Müller, "Theory, design and fabrication of a diffractive optical element," 2004.

[32] L. Hazra, "Diffractive optical elements: Past, present, and future," in *Selected Papers from International Conference on Optics and Optoelectronics' 98*, SPIE, vol. 3729, 1999, pp. 198–211.

[33] W. Lauterborn, T. Kurz, and M. Wiesenfeldt, "History of optics," in *Coherent Optics*, Springer, 1995, pp. 1–8.

[34] T. Young, "I. the bakerian lecture. experiments and calculations relative to physical optics," *Philosophical transactions of the Royal Society of London*, no. 94, pp. 1–16, 1804.

[35] P. A. T. Ryan, A. P. EllisCERN, C. Gough, *et al.*, "The double-slit experiment," *Physics World*, p. 15, 2002.

[36] A. Hessel, J. Schmoys, and D. Tseng, "Bragg-angle blazing of diffraction gratings," *JOSA*, vol. 65, no. 4, pp. 380–384, 1975.

[37] U. Levy, E. Marom, and D. Mendlovic, "Thin element approximation for the analysis of blazed gratings: Simplified model and validity limits," *Optics communications*, vol. 229, no. 1-6, pp. 11–21, 2004.

[38] X. Zheng, A. Lizana, A. Peinado, *et al.*, "Compact lcos–slm based polarization pattern beam generator," *Journal of Lightwave Technology*, vol. 33, no. 10, pp. 2047–2055, 2015.

[39] R. Fitzpatrick, *Maxwells Equations and the Principles of Electromagnetism*. Laxmi Publications, Ltd., 2010.

[40] B. Mahon, *The man who changed everything: The life of James Clerk Maxwell*. John Wiley & Sons, 2004.

[41] A. Forbes, *Laser beam propagation: generation and propagation of customized light*. CRC Press, 2014.

[42] H. Kogelnik and T. Li, "Laser beams and resonators," *Applied optics*, vol. 5, no. 10, pp. 1550–1567, 1966.

[43] D. L. Andrews, *Structured light and its applications: An introduction to phase-structured beams and nanoscale optical forces*. Academic press, 2011.

[44] L. Allen, M. W. Beijersbergen, R. Spreeuw, and J. Woerdman, "Orbital angular momentum of light and the transformation of laguerre-gaussian laser modes," *Physical review A*, vol. 45, no. 11, p. 8185, 1992.

[45] R. A. Beth, "Mechanical detection and measurement of the angular momentum of light," *Physical Review*, vol. 50, no. 2, p. 115, 1936.

[46] H. He, M. Friese, N. Heckenberg, and H. Rubinsztein-Dunlop, "Direct observation of transfer of angular momentum to absorptive particles from a laser beam with a phase singularity," *Physical review letters*, vol. 75, no. 5, p. 826, 1995.

[47] H. I. Sztul and R. R. Alfano, "The poynting vector and angular momentum of airy beams," *Optics express*, vol. 16, no. 13, pp. 9411–9416, 2008.

[48] R. Natarajan, *Power system capacitors*. CRC Press, 2018.

[49] R. Deshpande, *Capacitors: technology and trends*. Tata McGraw-Hill Education, 2012.

[50] M. Beijersbergen, R. Coerwinkel, M. Kristensen, and J. Woerdman, "Helical-wavefront laser beams produced with a spiral phaseplate," *Optics communications*, vol. 112, no. 5-6, pp. 321–327, 1994.

[51] V. V. Kotlyar, A. A. Almazov, S. N. Khonina, V. A. Soifer, H. Elfstrom, and J. Turunen, "Generation of phase singularity through diffracting a plane or gaussian beam by a spiral phase plate," *JOSA A*, vol. 22, no. 5, pp. 849–861, 2005.

[52] V. Y. Bazhenov, M. Vasnetsov, and M. Soskin, “Laser beams with screw dislocations in their wavefronts,” *Jetp Lett*, vol. 52, no. 8, pp. 429–431, 1990.

[53] M. Reicherter, T. Haist, E. Wagemann, and H. J. Tiziani, “Optical particle trapping with computer-generated holograms written on a liquid-crystal display,” *Optics letters*, vol. 24, no. 9, pp. 608–610, 1999.

[54] M. Harris, C. Hill, P. Tapster, and J. Vaughan, “Laser modes with helical wave fronts,” *Physical Review A*, vol. 49, no. 4, p. 3119, 1994.

[55] M. W. Beijersbergen, L. Allen, H. Van der Veen, and J. Woerdman, “Astigmatic laser mode converters and transfer of orbital angular momentum,” *Optics Communications*, vol. 96, no. 1-3, pp. 123–132, 1993.

[56] L. Marrucci, C. Manzo, and D. Paparo, “Optical spin-to-orbital angular momentum conversion in inhomogeneous anisotropic media,” *Physical review letters*, vol. 96, no. 16, p. 163 905, 2006.

[57] D. Naidoo, F. S. Roux, A. Dudley, *et al.*, “Controlled generation of higher-order poincaré sphere beams from a laser,” *Nature Photonics*, vol. 10, no. 5, pp. 327–332, 2016.

[58] N. Simpson, K. Dholakia, L. Allen, and M. Padgett, “Mechanical equivalence of spin and orbital angular momentum of light: An optical spanner,” *Optics letters*, vol. 22, no. 1, pp. 52–54, 1997.

[59] J. Wang, J.-Y. Yang, I. M. Fazal, *et al.*, “Terabit free-space data transmission employing orbital angular momentum multiplexing,” *Nature photonics*, vol. 6, no. 7, pp. 488–496, 2012.

[60] N. Bozinovic, Y. Yue, Y. Ren, *et al.*, “Terabit-scale orbital angular momentum mode division multiplexing in fibers,” *Science*, vol. 340, no. 6140, pp. 1545–1548, 2013.

[61] G. Vallone, V. D’Ambrosio, A. Sponselli, *et al.*, “Free-space quantum key distribution by rotation-invariant twisted photons,” *Physical review letters*, vol. 113, no. 6, p. 060 503, 2014.

[62] L. Torner, J. P. Torres, and S. Carrasco, “Digital spiral imaging,” *Optics express*, vol. 13, no. 3, pp. 873–881, 2005.

[63] J. Courtial, K. Dholakia, L. Allen, and M. Padgett, “Second-harmonic generation and the conservation of orbital angular momentum with high-order laguerre-gaussian modes,” *Physical Review A*, vol. 56, no. 5, p. 4193, 1997.

[64] D. McGloin and K. Dholakia, “Bessel beams: Diffraction in a new light,” *Contemporary physics*, vol. 46, no. 1, pp. 15–28, 2005.

[65] J. Durnin, “Exact solutions for nondiffracting beams. i. the scalar theory,” *JOSA A*, vol. 4, no. 4, pp. 651–654, 1987.

[66] F. Gori, G. Guattari, and C. Padovani, “Bessel-gauss beams,” *Optics communications*, vol. 64, no. 6, pp. 491–495, 1987.

[67] V. Bagini, F. Frezza, M. Santarsiero, G. Schettini, and G. S. Spagnolo, “Generalized bessel-gauss beams,” *Journal of modern optics*, vol. 43, no. 6, pp. 1155–1166, 1996.

[68] J. Durnin, J. Miceli Jr, and J. H. Eberly, “Diffraction-free beams,” *Physical review letters*, vol. 58, no. 15, p. 1499, 1987.

[69] O. Brzobohat, T. Čižmár, and P. Zemánek, "High quality quasi-bessel beam generated by round-tip axicon," *Optics express*, vol. 16, no. 17, pp. 12 688–12 700, 2008.

[70] A. Vasara, J. Turunen, and A. T. Friberg, "Realization of general nondiffracting beams with computer-generated holograms," *JOSA A*, vol. 6, no. 11, pp. 1748–1754, 1989.

[71] S. Tao, W. Lee, and X.-C. Yuan, "Dynamic optical manipulation with a higher-order fractional bessel beam generated from a spatial light modulator," *Optics letters*, vol. 28, no. 20, pp. 1867–1869, 2003.

[72] J. Arlt and K. Dholakia, "Generation of high-order bessel beams by use of an axicon," *Optics Communications*, vol. 177, no. 1-6, pp. 297–301, 2000.

[73] Z. Wang, S. Dong, W. Luo, *et al.*, "High-efficiency generation of bessel beams with transmissive metasurfaces," *Applied Physics Letters*, vol. 112, no. 19, p. 191 901, 2018.

[74] D. McGloin, V. Garcés-Chávez, and K. Dholakia, "Interfering bessel beams for optical micromanipulation," *Optics letters*, vol. 28, no. 8, pp. 657–659, 2003.

[75] G. B. Airy *et al.*, "On the intensity of light in the neighbourhood of a caustic," *Transactions of the Cambridge Philosophical Society*, vol. 6, p. 379, 1838.

[76] M. V. Berry and N. L. Balazs, "Nonspreading wave packets," *American Journal of Physics*, vol. 47, no. 3, pp. 264–267, 1979.

[77] X. Chu, G. Zhou, and R. Chen, "Analytical study of the self-healing property of airy beams," *Physical Review A*, vol. 85, no. 1, p. 013 815, 2012.

[78] G. A. Siviloglou and D. N. Christodoulides, "Accelerating finite energy airy beams," *Optics letters*, vol. 32, no. 8, pp. 979–981, 2007.

[79] G. Porat, I. Dolev, O. Barlev, and A. Arie, "Airy beam laser," *Optics letters*, vol. 36, no. 20, pp. 4119–4121, 2011.

[80] J. Kasparian and J.-P. Wolf, "Laser beams take a curve," *Science*, vol. 324, no. 5924, pp. 194–195, 2009.

[81] G. Siviloglou, J. Broky, A. Dogariu, and D. Christodoulides, "Ballistic dynamics of airy beams," *Optics Letters*, vol. 33, no. 3, pp. 207–209, 2008.

[82] J. Baumgartl, M. Mazilu, and K. Dholakia, "Optically mediated particle clearing using airy wavepackets," *Nature photonics*, vol. 2, no. 11, pp. 675–678, 2008.

[83] P. Zhang, J. Prakash, Z. Zhang, *et al.*, "Trapping and guiding microparticles with morphing autofocusing airy beams," *Optics letters*, vol. 36, no. 15, pp. 2883–2885, 2011.

[84] Z. Zheng, B.-F. Zhang, H. Chen, J. Ding, and H.-T. Wang, "Optical trapping with focused airy beams," *Applied optics*, vol. 50, no. 1, pp. 43–49, 2011.

[85] P. Polynkin, M. Kolesik, J. V. Moloney, G. A. Siviloglou, and D. N. Christodoulides, "Curved plasma channel generation using ultraintense airy beams," *Science*, vol. 324, no. 5924, pp. 229–232, 2009.

[86] A. Salandrino and D. N. Christodoulides, "Airy plasmon: A nondiffracting surface wave," *Optics letters*, vol. 35, no. 12, pp. 2082–2084, 2010.

[87] D. L. Shealy and J. A. Hoffnagle, "Laser beam shaping profiles and propagation," *Applied optics*, vol. 45, no. 21, pp. 5118–5131, 2006.

[88] D. L. Simms, "Archimedes and the burning mirrors of syracuse," *Technology and Culture*, vol. 18, no. 1, pp. 1–24, 1977.

[89] A. C. Claus, "On archimedes' burning glass," *Applied Optics*, vol. 12, no. 10, A14–A14, 1973.

[90] O. Stavroudis, "Comments on: On archimedes' burning glass," *Applied Optics*, vol. 12, no. 10, A16–A16, 1973.

[91] T. H. Maiman, T. H. Maiman, and Holland, *Laser Inventor*. Springer, 2018.

[92] F. M. Dickey, "Laser beam shaping," *Optics and photonics news*, vol. 14, no. 4, pp. 30–35, 2003.

[93] F. M. Dickey, L. S. Weichman, and R. N. Shagam, "Laser beam shaping techniques," in *High-Power Laser Ablation III*, International Society for Optics and Photonics, vol. 4065, 2000, pp. 338–348.

[94] P. Blair, M. Currie, N. Trela, *et al.*, "Field mappers for laser material processing," in *Laser Resonators, Microresonators, and Beam Control XVIII*, SPIE, vol. 9727, 2016, pp. 77–86.

[95] B. R. Frieden, "Lossless conversion of a plane laser wave to a plane wave of uniform irradiance," *Applied Optics*, vol. 4, no. 11, pp. 1400–1403, 1965.

[96] O. Bryngdahl, "Optical map transformations," *Optics Communications*, vol. 10, no. 2, pp. 164–168, 1974.

[97] O. Bryngdahl., "Geometrical transformations in optics," *JOSA*, vol. 64, no. 8, pp. 1092–1099, 1974.

[98] J. L. Kreuzer, *Coherent light optical system yielding an output beam of desired intensity distribution at a desired equiphase surface*, US Patent 3,476,463, Nov. 1969.

[99] R. Li and L. Cao, "Progress in phase calibration for liquid crystal spatial light modulators," *Applied Sciences*, vol. 9, no. 10, p. 2012, 2019.

[100] Z. Zhang, Z. You, and D. Chu, "Fundamentals of phase-only liquid crystal on silicon (lcos) devices," *Light: Science & Applications*, vol. 3, no. 10, e213–e213, 2014.

[101] D. P. Sprünken, "A 2d spatial light modulator for spatio-temporal shaping," M.S. thesis, University of Twente, 2008.

[102] D. Dudley, W. M. Duncan, and J. Slaughter, "Emerging digital micromirror device (dmd) applications," in *MOEMS display and imaging systems*, SPIE, vol. 4985, 2003, pp. 14–25.

[103] M. Pivnenko, K. Li, and D. Chu, "Sub-millisecond switching of multi-level liquid crystal on silicon spatial light modulators for increased information bandwidth," *Optics Express*, vol. 29, no. 16, pp. 24 614–24 628, 2021.

[104] Y. Wang, G. Zhou, X. Zhang, *et al.*, "2d broadband beamsteering with large-scale mems optical phased array," *Optica*, vol. 6, no. 5, pp. 557–562, 2019.

[105] R. Ketchum and P. Blanche, *Diffraction efficiency characteristics for mems-based phase-only spatial light modulator with nonlinear phase distribution. photonics 2021, 8, 62*, 2021.

[106] J. Shane, R. Serati, H. Masterson, and S. Serati, "A holographic optical tweezers module for the international space station," in *Optical Trapping and Optical Micromanipulation XIII*, SPIE, vol. 9922, 2016, pp. 220–232.

[107] Holoeye. "Holoeye phase-only slm." (2022), [Online]. Available: https://holoeye.com/slm-pluto-phase-only/.

[108] E. Palmer, M. Hutley, A. Franks, J. Verrill, and B. Gale, "Diffraction gratings (manufacture)," *Reports on Progress in Physics*, vol. 38, no. 8, p. 975, 1975.

[109] M. A. Golub, "Laser beam splitting by diffractive optics," *Optics and Photonics News*, vol. 15, no. 2, pp. 36–41, 2004.

[110] C. Palmer and E. G. Loewen, "Diffraction grating handbook," 2005.

[111] J. E. Harvey and R. N. Pfisterer, "Understanding diffraction grating behavior: Including conical diffraction and rayleigh anomalies from transmission gratings," *Optical Engineering*, vol. 58, no. 8, p. 087 105, 2019.

[112] C. Rosales-Guzmán, N. Bhebhe, N. Mahonisi, and A. Forbes, "Multiplexing 200 spatial modes with a single hologram," *Journal of Optics*, vol. 19, no. 11, p. 113 501, 2017.

[113] V. Arrizón, U. Ruiz, R. Carrada, and L. A. González, "Pixelated phase computer holograms for the accurate encoding of scalar complex fields," *JOSA A*, vol. 24, no. 11, pp. 3500–3507, 2007.

[114] B. Sephton, A. Dudley, and A. Forbes, "Revealing the radial modes in vortex beams," *Applied optics*, vol. 55, no. 28, pp. 7830–7835, 2016.

[115] Roddier, *Adaptive optics in astronomy*. Cambridge university press, 1999.

[116] L. Burger, I. A. Litvin, and A. Forbes, "Simulating atmospheric turbulence using a phase-only spatial light modulator," *South African Journal of Science*, vol. 104, no. 3, pp. 129–134, 2008.

[117] C. Sterken and J. Manfroid, "Atmospheric turbulence: Scintillation and seeing," in *Astronomical Photometry*, Springer, 1992, pp. 111–117.

[118] D. J. Schroeder, *Astronomical optics*. Elsevier, 1999.

[119] A. Gover, *Encyclopedia of modern optics*, 2005.

[120] M. D. Al-Amri, D. L. Andrews, and M. Babiker, *Structured Light for Optical Communication*. Elsevier, 2021.

[121] H. W. Babcock, "The possibility of compensating astronomical seeing," *Publications of the Astronomical Society of the Pacific*, vol. 65, no. 386, pp. 229–236, 1953.

[122] P.-Y. Madec, "Overview of deformable mirror technologies for adaptive optics and astronomy," in *Adaptive Optics Systems III*, International Society for Optics and Photonics, vol. 8447, 2012, p. 844 705.

[123] F. J. Roddier, J. Anuskiewicz, J. E. Graves, M. J. Northcott, and C. A. Roddier, "Adaptive optics at the university of hawaii i: Current performance at the telescope," in *Adaptive Optics in Astronomy*, SPIE, vol. 2201, 1994, pp. 2–9.

[124] G. Vdovin, M. Loktev, and A. Simonov, "Low-cost deformable mirrors: Technologies and goals," in *Advanced Wavefront Control: Methods, Devices, and Applications III*, International Society for Optics and Photonics, vol. 5894, 2005, 58940B.

[125] R. Dahiya and M. Valle, *Appendix a fundamentals of piezoelectricity. robotic tactile sensing*, 2013.

[126] S. Manzanera, M. A. Helmbrecht, C. J. Kempf, and A. Roorda, "Mems segmented-based adaptive optics scanning laser ophthalmoscope," *Biomedical optics express*, vol. 2, no. 5, pp. 1204–1217, 2011.

[127] R. K. Tyson, *Adaptive optics engineering handbook*. Marcel Dekker New York, 2000.

[128] F. Hopkinson and D. Rittenhouse, "An optical problem, proposed by mr. hopkinson, and solved by mr. rittenhouse," *Transactions of the American Philosophical Society*, vol. 2, pp. 201–206, 1786.

[129] A. Leitner, "The life and work of joseph fraunhofer (1787- 1826)," *American Journal of Physics*, vol. 43, no. 1, pp. 59–68, 1975.

[130] I. V. Minin and O. V. Minin, "Fresnel zone plate lens and antennas for millimeter waves: History and evolutions of developments and applications," in *25th International Conference on Infrared and Millimeter Waves (Cat. No. 00EX442)*, IEEE, 2000, pp. 409–410.

[131] R. W. Wood, "Liii. phase-reversal zone-plates, and diffraction-telescopes," *The London, Edinburgh, and Dublin Philosophical Magazine and Journal of Science*, vol. 45, no. 277, pp. 511–522, 1898.

[132] A. Tudorovskii, "An objective with a phase plate," *Optics and Spectroscopy*, vol. 6, p. 126, 1959.

[133] K. Miyamoto, "The phase fresnel lens," *JOSA*, vol. 51, no. 1, pp. 17–20, 1961.

[134] G. L. Rogers, "Gabor diffraction microscopy: The hologram as a generalized zone-plate," *Nature*, vol. 166, no. 4214, pp. 237–237, 1950.

[135] L. d'Auria, J. Huignard, A. Roy, and E. Spitz, "Photolithographic fabrication of thin film lenses," *Optics communications*, vol. 5, no. 4, pp. 232–235, 1972.

[136] J.-J. Clair, "New methods to synthesise kinoforms," *Optics Communications*, vol. 6, no. 2, pp. 135–137, 1972.

[137] A. W. Lohmann and D. Paris, "Binary fraunhofer holograms, generated by computer," *Applied optics*, vol. 6, no. 10, pp. 1739–1748, 1967.

[138] W. B. Veldkamp and G. J. Swanson, "Developments in fabrication of binary optical elements," in *Intl Conf on Computer-Generated Holography*, International Society for Optics and Photonics, vol. 437, 1983, pp. 54–59.

[139] H. S. Lee, B. Stewart, K. Choi, and H. Fenichel, "Holographic nondiverging hollow beam," *Physical Review A*, vol. 49, no. 6, p. 4922, 1994.

[140] D. Dravins, L. Lindegren, E. MEzEY, and A. T. Young, "Atmospheric intensity scintillation of stars. iii. effects for different telescope apertures," *Publications of the Astronomical Society of the Pacific*, vol. 110, no. 747, p. 610, 1998.

[141] F. Roddier, "Historical context," *Adaptive Optics in Astronomy*, pp. 3–7, 1999.

[142] R. K. Tyson and B. W. Frazier, *Principles of adaptive optics*. CRC press, 2022.

[143] E. I. Sponable, "Eidophor system of theater television," *Journal of the Society of Motion Picture and Television Engineers*, vol. 60, no. 4, pp. 337–343, 1953.

[144] E. Labin, "The eidophor method for theater television," *Journal of the Society of Motion Picture and Television Engineers*, vol. 54, no. 4, pp. 393–406, 1950.

[145] R. Freeman and J. E. Pearson, "Deformable mirrors for all seasons and reasons," *Applied Optics*, vol. 21, no. 4, pp. 580–588, 1982.

[146] S. C. Gustafson, G. R. Little, T. A. Rhoadarmer, and T. A. Tuthill, "Communication applications for deformable mirror devices.," 1997.

[147] A. Tuantranont and V. M. Bright, “Segmented silicon-micromachined microelectromechanical deformable mirrors for adaptive optics,” *IEEE Journal of selected topics in quantum electronics*, vol. 8, no. 1, pp. 33–45, 2002.

[148] M. A. Helmbrecht, T. Juneau, M. Hart, and N. Doble, “Segmented mems deformable-mirror technology for space applications,” in *Micro (MEMS) and Nanotechnologies for Space Applications*, SPIE, vol. 6223, 2006, pp. 25–31.

[149] R. K. Tyson, M. Scipioni, and J. Viegas, “Generation of an optical vortex with a segmented deformable mirror,” *Applied optics*, vol. 47, no. 33, pp. 6300–6306, 2008.

[150] X. Yu, A. Todi, and H. Tang, “Bessel beam generation using a segmented deformable mirror,” *Applied Optics*, vol. 57, no. 16, pp. 4677–4682, 2018.